Bioactive Materials 40 (2024) 524–540

Contents lists available at ScienceDirect

Bioactive Materials

journal homepage: www.keaipublishing.com/en/journals/bioactive-materials

Study of the effect of magnetic fields on static degradation of Fe and Fe-12Mn-1.2C in balanced salts modified Hanks' solution

Irene Limón [a], Marta Multigner [a,*], Carlo Paternoster [b], Marcela Lieblich [c], Belén Torres [a], Diego Mantovani [b], Joaquín Rams [a]

[a] Dpto. de Matemática Aplicada, Ciencia e Ingeniería de Materiales y Tecnología Electrónica, ESCET, Universidad Rey Juan Carlos, Tulipán S/n, 28933, Móstoles, Madrid, Spain
[b] Laboratory for Biomaterials and Bioengineering, Dept of Min-Met-Materials Engineering, Laval University & University Hospital Research Center, Quebec City, Canada
[c] Centro Nacional de Investigaciones Metalúrgicas (CENIM-CSIC), 28040, Madrid, Spain

ARTICLE INFO

Keywords:
Biometals
Biodegradable iron alloy
Corrosion
Magnetic fields
Biodegradable implant
Magnetohydrodynamics

ABSTRACT

Iron and its alloys are attractive as biodegradable materials because of their low toxicity and suitable mechanical properties; however, they generally have a slow degradation rate. Given that corrosion is an electrochemical phenomenon where an exchange of electrons takes place, the application of magnetic fields from outside the body may accelerate the degradation of a ferrous temporary implant. In the present study, we have investigated the effect of alternating and direct low magnetic field (H = 6.5 kA/m) on the corrosion process of pure iron (Fe) and an iron-manganese alloy (FeMnC) in modified Hanks' solution. A 14-day static immersion test was performed on the materials. The corrosion rate was assessed by mass and cross-sectional loss measurements, scanning electron microscopy, X-ray diffractometry, Fourier-transform infrared spectroscopy and X-ray photoelectron spectroscopy before and after degradation. The results show that the presence of magnetic fields significantly accelerates the degradation rate of both materials, with the corrosion rate being twice as high in the case of Fe and almost three times as high for FeMnC. In addition, a homogenous degradation layer is formed over the entire surface and the chemical composition of the degradation products is the same regardless of the presence of a magnetic field.

1. Introduction

Cardiovascular disease is the leading cause of death worldwide [1]. Atherosclerosis, the narrowing of the coronary arteries caused by blood substances accumulating in the artery walls, has a high prevalence [2]. A common surgical procedure is angioplasty, which consists of the insertion of a stent that provides mechanical support as a vascular scaffold to restore and maintain blood flow in the vessels [3,4]. However, the implantation of a permanent stent has some limitations, such as long-term endothelial dysfunction, permanent physical irritation and, in some cases, if a second clinical intervention is required, the presence of the stent represents an additional difficulty. Because of these limitations, temporary implants have gained interest in cardiovascular applications in recent years [5–7]. To illustrate their growing importance, the global coronary stent market is expected to grow at a compound annual growth rate (CAGR) of 4.78 %, reaching $8.56 billion in 2021 and $13.03 billion in 2030 [8]. In fact, the bioabsorbable stent market is expected to reach $532 million by 2029 at a CAGR of 7.35 % during the forecast period (2023–2029) [9].

Bioabsorbable stents based on two types of materials, polymers and metals, have been the subject of numerous clinical and preclinical studies [10]. Although polymeric stents have shown promising results, they also have some disadvantages that limit their use. Compared to metals, polymers have lower Young's modulus values (0.2–7.0 GPa for polymers versus 54–200 GPa for metals) and generally inferior mechanical properties [3]. As a result, the struts in polymer stents need to be thicker than in metallic ones. In addition, incomplete balloon expansion can occur during the procedure due to elastic recoil [11]. Metals can overcome these challenges due to their higher yield strength and ductility, in particular Fe, Mg, Zn and their alloys have emerged as

Peer review under responsibility of KeAi Communications Co., Ltd.
* Corresponding author.
E-mail addresses: irene.limon@urjc.es (I. Limón), marta.multigner@urjc.es (M. Multigner), carlo.paternoster.ulaval1@gmail.com (C. Paternoster), marcela@cenim.csic.es (M. Lieblich), belen.torres@urjc.es (B. Torres), diego.mantovani@gmn.ulaval.ca (D. Mantovani), joaquin.rams@urjc.es (J. Rams).

https://doi.org/10.1016/j.bioactmat.2024.06.027
Received 31 January 2024; Received in revised form 18 June 2024; Accepted 18 June 2024

potential materials for the manufacture of biodegradable cardiovascular implants [12].

Today, the only commercially available metallic biodegradable cardiovascular stents are made of Mg-based alloys (Magmaris, Biotronik) [13]. They were the result of intensive prior research over the last two decades aimed at improving the mechanical and chemical properties of Mg by increasing its yield strength and elongation, and homogenising and reducing its corrosion, thereby decreasing hydrogen release [13–15]. Despite the successful experiments with the aforementioned devices, scientific research is still ongoing to overcome challenges such as reducing the thickness of the strut stent while maintaining suitable mechanical properties for the final application [16]. In this sense, Zn and Fe are expected to have higher mechanical performance than Mg. Zn and its alloys have good biocompatibility and adequate corrosion rate, but their mechanical properties still need to be improved [12,17,18]. Fe-based alloys have mechanical properties close to those of other performant alloys, like Co-Cr or AISI 316L. These properties, together with the fact that the degradation products of resorbable Fe-based alloys are mostly biocompatible [19], make this group of metallic materials an interesting candidate for stent applications [20–22]. Furthermore, some in vivo studies have shown no restenosis, no marked inflammation and no local or systemic toxicity of pure iron stents [23–25]. However, the degradation rate of Fe is too slow for this application [19]. For this reason, researchers have proposed several methods to increase its degradation rate: alloying [7,20,26,27], surface modification [28,29] and new fabrication methods responsible for microstructural modifications [30–32]. In particular, Fe-Mn alloys have gained interest in recent years because Mn accelerates the degradation process of Fe-based alloys. At the same time, it stabilizes the austenitic phase, which is not ferromagnetic, and is compatible with magnetic resonance imaging techniques [33–35]. At this point, it is worth mentioning the controversy around the use of ferromagnetic materials in implants due to risks of implant displacement, temperature rise and image artifacts during magnetic resonance imaging (MRI). These potential risks should be carefully assessed, and the safety of the implants should be guaranteed, as it may happen that the implant is not MRI compatible before partial or total degradation [36]. If that happens, it does not mean that said implant should be discarded, but that MRI should be avoided until the implant is sufficiently degraded. MRI restrictions are common for some other widely used implants, such as pacemakers, where the use of MRI is limited and other imaging techniques, i.e. those based on X-rays, are usually recommended.

In recent times, the effect of direct magnetic fields on aqueous corrosion of different materials has been studied [32,36–38]. Some authors reported that magnetic fields cause a decrease in the corrosion rates of metals such as Cu and Fe in nitric acid [40], or pure iron in sulfate and chloride solutions [32], however other studies reported an increase in corrosion rate by applying magnetic fields, for example, AISI 303 in $FeCl_3$ solution [32]. Without considering the materials, the medium or the magnetic field amplitude, these studies clearly showed that direct magnetic fields have some effects on the electrochemical processes. The different behaviors were explained in terms of the forces exerted by the magnetic field on the electrical charges involved in the corrosion process. The effect of low frequency alternating electromagnetic fields on corrosion is much less well documented. Recent work has proposed the use of the alternating magnetic field as an anticorrosion system by adjusting the electric charge on the surface of the metallic system thanks to the induced currents [41].

Research on the effects of exposure to a magnetic field during corrosion in physiological environments is limited. The existing research mainly focuses on magnetic materials that produce movement inside the body due to their magnetostrictive properties. For example, smart magnetic materials (SMMs) such as Ni-Mn-Ga and Tb-Dy-Fe alloys exhibit susceptibility to corrosion when placed in a magnetic field. This requires the use of protective coatings for medical applications due to their lack of biocompatibility [42]. The use of magnetic fields during the degradation process of cardiovascular stents for the modification of the corrosion rate of the ferrous material was first proposed in 2019 [43]. The research demonstrated that a 10 mT field increases the corrosion rate of both iron and an iron-manganese alloy. On the other hand, in 2023, the use of direct magnetic fields to accelerate the degradation of a FeGa alloy for orthopedic applications was reported, where an increase of the corrosion rate using 60-mT magnetic field was observed [44].

The aim of this investigation is to determine whether low-intensity magnetic fields can alter the corrosion rate of ferrous alloys without affecting their biocompatibility. This could potentially be used as a non-invasive technique to enhance the degradation rate of cardiovascular stents. To this end, the effect of direct and alternating magnetic fields on the degradation behavior in modified Hanks' solution of pure Fe and Fe12Mn1.2C (% wt.) has been studied following a 14-day assay. These two materials have been chosen as representatives of different magnetic behaviors, namely ferromagnetic and paramagnetic. They are also being extensively researched for their potential use in non-permanent cardiovascular stents. This research is focused on the effect of magnetic fields on the corrosion rate, the corrosion layers and the nature of the corrosion products as a function of type of magnetic field (DC, AC) and material (Fe and Fe12Mn1.2C).

2. Experimental procedure

2.1. Starting materials

The materials studied were pure ferromagnetic Fe (99.8 % ARMCO®, Mn < 800 ppm, C < 200pp, P < 200 ppm, S < 150 ppm, rolled, Goodfellow) and paramagnetic austenitic steel (12 % Mn, 1.2 % C, 1 % Si, P < 700 ppm) [35,45], hereinafter named as FeMn. All the samples had a size of 14 × 7 × 1 mm^3. The Fe specimens underwent heat treatment at 650 °C for 1 h, while the FeMn samples were annealed at 850 °C for 1 h to relieve any residual stress. The samples were grinded, polished with diamond paste up to 1 μm of granulometry, and rinsed with deionized water and ethanol, according to the standard metallographic procedure for metallic specimens.

For microstructure assessment, the samples were etched with Nital (2 %) solution to reveal the microstructure, which was characterized by scanning electron microscopy (SEM). The sample surfaces were studied in their as-received condition and after chemical etching using a Hitachi S-3400 N microscope with a W filament, a 15 kV bias, and a filament current of 60 μA. The grain size distribution was calculated based on 3 micrographs using image analysis (ImageJ), taking 100 measurements for each one. The data are represented as mean ± SD (Standard Deviation). The surface chemical composition was assessed with an energy dispersive X-ray spectrometer (EDS, Bruker AXS Xflash Detector 5010, Bruker AXS Microanalysis, Berlin, Germany) operated under a vacuum of $1.5{\cdot}10^{-3}$ Torr. No metallization was performed on the samples after the degradation test.

2.2. Degradation test

The degradation behavior of the Fe and FeMn samples during static immersion degradation test in a balanced salt modified Hanks' solution was evaluated accordingly to *ASTM G31*: *Standard Guide for Laboratory Immersion Corrosion Testing of Metals* [46]. The specimen surface was prepared according to the procedure previously described in section 2.1.

The used medium for the degradation test was a modified Hanks' solution, already proposed by other authors [47,48]. The medium (Sigma-Aldrich H1387) is composed of 0.185 g/L of dihydrate CaCl2, 0.09767 g/L of anhydrous MgSO4, 0.4 g/L of KCl, 0.06 g/L of anhydrous KH2PO4, 8.0 g/L of NaCl, 0.04788 g/L of anhydrous Na_2HPO_4 and 1.0 g/L of D-glucose, which was supplemented with 10.11 g/L HEPES buffer $C_8H_{17}N_2NaO_4S$ (Sigma 3375), 11.89 g/L HEPES sodium salt (Sigma 7006) and 2.34 g/L sodium bicarbonate $NaHCO_3$ (Sigma 5761). The salts were dissolved in 1 L of deionized water at T = 23 °C and stirred for

t = 30 min. The pH of the solution was adjusted to 7.4, by adding small amounts of HCl 1 M or NaOH 1 M, as appropriate.

Each sample was suspended with a nylon thread and placed in the center of a 50-mL conical tube (Falcon ™) kept in vertical position, after autoclave sterilization. The test had a duration of 14 days in an environmental chamber with a temperature T = 37±1 °C. The minimal amount of medium was calculated on the basis of A STM G31 standard [46], and equal to 0.20 mL/mm^2.

Degradation tests were performed in the absence of a magnetic field (H0), under a 50 Hz alternating magnetic field (AC), and under a direct magnetic field (DC).

2.3. Experimental setup of degradation tests

Three samples were tested for each of the three conditions. Table 1 lists the nomenclature applied to each sample and testing condition.

A coil was placed around each Falcon tube; the setup scheme for each kind of superposed magnetic field is presented in Fig. 1. Copper coils were composed by 600 windings with an internal diameter of 35 mm, and an axial length of 60 mm. The field in the middle of the coil, where the sample was positioned, was calibrated by a longitudinal Hall probe (HIRST GM-08) resulting in a coil constant of 6500 A/m/A.

For AC field experiments, an AC variable voltage transformer plugged to a wall socket (50 Hz) and a variable resistor were used to feed three coils in series (Fig. 1b) with 1 A current that was measured with a multimeter (DT9205A Silver Electronics). During the tests the peak amplitude for 50 Hz AC was H = 6500 A/m. Likewise, it should be pointed out that the intensity of the magnetic field used in the present work is two orders of magnitude lower than those used in MRI and no movement nor temperature increase of the samples have been observed.

For DC field experiments, a DC power source (PeakTech P6226) was used to feed the three coils with 1 A (Fig. 1c). During the tests the field in the middle of the coil was H = 6500 A/m.

2.4. Simulation with FEM

To simulate the magnetic field in and around the samples during the tests by finite element modeling methods, the free software package FEMM [49] was used. In the pre-processing stage, the magnetizing system model was designed with the actual units of length, which is a three-dimensional magnetic coil, and the sample was simplified into a two-dimensional problem (0.7 mm × 14 mm x infinite depth). The software library's materials properties were assigned to a pure Fe sample and a copper wire coil (10 AWG). For FeMn, the data obtained from the hysteresis loop were manually added to the system. Coil dimensions and experimental parameters were replicated in the simulations (35 mm of internal diameter, 60 mm axial length, 600 turns and 1 A as excitation current).

2.5. Corrosion rate evaluation

At the end of each test, the specimens were removed from the solution. Once extracted, the samples were washed several times with a 70 vol % ethanol solution in an ultrasonic bath (10 min). The weight of the samples was measured after each wash. The cleaning ended when the weight difference between two consecutive weightings was less than 1 mg.

The testing medium, composed by a supernatant and the solid degradation product detached during the test, hereinafter named as *detached products* (DP), was centrifuged, Fig. 2 a. The DP were then extracted, put in ~10 mL 70 vol % ethanol solution, vortexed, and centrifuged again. The liquid gathered during cleaning was centrifuged and the loose degradation products were collected and dried, hereinafter named as *removed products* (RP), Fig. 2 b. Both RPs and DPs were then put together, and kept in a desiccator until further characterization.

The weight loss method was used to calculate corrosion rates, following the equation (eq. (1)):

$$CR = 8.74 \cdot 10^4 \frac{W}{At\rho} \quad (1)$$

Where CR is the corrosion rate (mm year^{-1}), W is the weight loss (g), A is the exposed area (cm^2), t is the exposure time (hours) and ρ is the material density (g·cm^{-3}). 8.74·10^4 (mm.hours cm^{-1}.year^{-1}) is the conversion constant to obtain the corrosion rate in mm/year [50]. The results of mass loss and corresponding corrosion rates are represented as mean ± standard deviation of the three samples for each condition.

In addition, in the FeMnC samples, the corrosion rate was also quantified by calculating the material loss through the reduction of thickness of their cross sections [51,52]. For carrying this out, samples cross-sections were metallographically prepared and measured on SEM micrographs at 50 points. The data are represented as mean ± SD. ANOVAs with Tukey's correction were used to compare between conditions. The p-value <0.05 was considered to be statistically significant.

2.6. Characterization of degraded samples and corrosion products

Both parallel and perpendicular surfaces to the magnetic field were analyzed for each material and condition. The microstructure was observed using SEM (section 2.1). The sample cross sections were prepared preserving the attached corrosion product layer, for which purpose samples were electrolytically coated with a thin layer of Cu. The electrodeposition was carried out in an electrolyte solution consisting of 2.2 g $CuSO_4 \cdot 5H_2O$ (Sigma-Aldrich), 3.3 mL H_2SO_4 (Sigma-Aldrich) in 100 mL of distilled water. The corroded samples were immersed in a solution, and a current was applied, causing copper ions to deposit onto the corroded layer [53]. After cutting, specimens were mounted in resin, mechanically polished with up to 1 μm diamond paste and ultrasonically cleaned.

The chemical composition of the surface of the samples was analyzed using an X-ray photoelectron spectroscopy (XPS) platform (PHI 5600-ci, Physical Electronics, Chanhassen, MN, USA). A survey spectrum covering the range of 0–1400 eV (Al anode) and high-resolution spectra for the C1s, O1s, Fe2p, and Mn2p regions were recorded with achromatic radiation. The least squares method was used to perform curve fitting with PHI MultiPak™ software and Gaussian-Lorentz (30–70)

Table 1
Materials and conditions of the specimens.

	Condition		*Position of sample surface*			
	Fe ARMCO	Fe-12Mn-1.2C		Fe ARMCO	Fe-12Mn-1.2C	
As-received	-	-	parallel surface to the gravitational field	Fe-P	FM-P	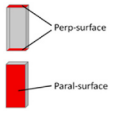
			perpendicular surface to the gravitational field	Fe-C	FM-C	
No magnetic field	FeH0	FMH0	parallel surface to applied ***H***	FeH0-P	FMH0-P	
			perpendicular surface to applied ***H***	FeH0-C	FMH0-C	
AC magnetic field	FeAC	FMAC	parallel surface to applied ***H***	FeAC-P	FMAC-P	
			perpendicular surface to applied ***H***	FeAC-C	FMAC-C	
DC magnetic field	FeDC	FMDC	parallel surface to applied ***H***	FeDC-P	FMDC-P	
			perpendicular surface to applied ***H***	FeDC-C	FMDC-C	

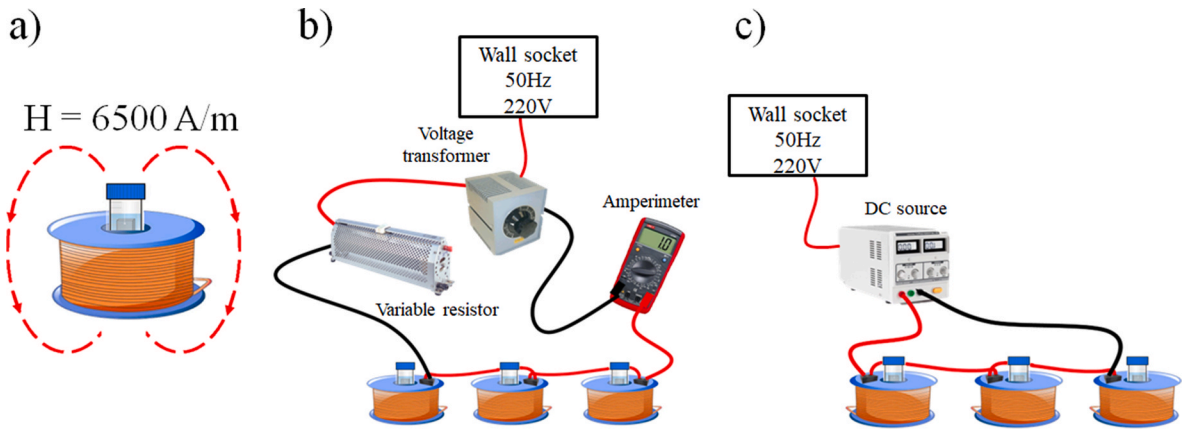

Fig. 1. Magnetic experimental setup: (a) sample and coil arrangement (b) AC and (c) DC setup.

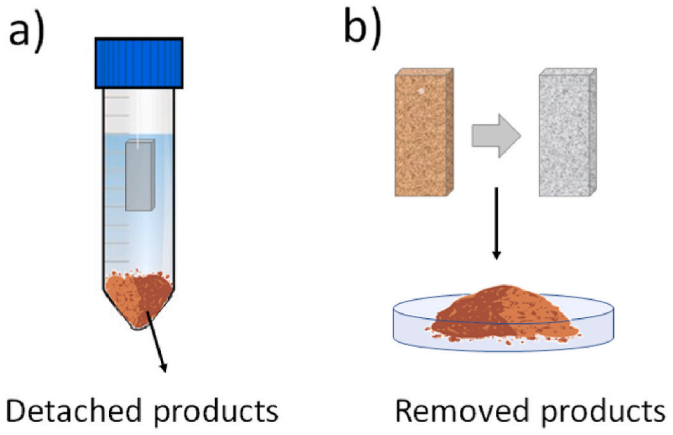

Fig. 2. Degradation products: a) detached during the corrosion test and b) removed during the cleaning process.

functions.

The corrosion products that spontaneously detached during the degradation test as well as those collected from the cleaning process of the sample were analyzed by Fourier infrared spectroscopy (FTIR, Pekin Elmer/Spectrum 100). XRD patterns of the degradation products were obtained only for magnetic field conditions because the amount of corrosion products was insufficient for this technique without a magnetic field. A Bruker AXS D8 diffractometer (Bruker, Billerica, MA, USA) equipped with a Co X-ray ($\lambda_{K\alpha} = 1.7902$ Å) tube working at a current of 30 mA and a voltage of 40 kV, was used. The data were collected over a 2θ range from 10° to 120° with a step size of 0.015° and a step time of 288 s, using a θ-2θ configuration. It is worth noticing that Co radiation was used to minimize the effect of Fe background fluorescence.

3. Results

3.1. As-received specimens

Fig. 3 shows micrographs of parallel and cross sections of Fe and FeMn as-received samples: Fe-P, Fe-C, FM-P and FM-C (Table 1). The grain size of Fe-P and Fe-C are 30.6 ± 12.6 μm and 45.7 ± 28.7 μm, respectively. The features observed inside the grains of Fe-P are attributed to different grain orientation [54]. The microstructures of FM-C and FM-P are similar and composed mainly of small equiaxed grains with average grain sizes of 8.8 ± 4.5 μm in FM-P and 8.4 ± 3.6 μm in FM-C. Precipitates were observed at grain boundaries in both cases, which were identified by EDX as iron carbides.

3.2. Magnetic characterization

Fig. 4 displays the hysteresis loop for pure Fe and FeMn samples when a maximum field of 10 kA/m is applied parallel to the long direction. Due to the short dimension of the samples, the magnetic shape anisotropy hinders the saturation magnetization, and B presents an almost linear dependence with H. Pure Fe samples, a relative magnetic permeability of $\mu_r = 2.98$ was measured. The FeMn samples perform as a typical paramagnetic material with a relative magnetic permeability of $\mu_r = 1.93$.

3.3. Degraded samples

Fig. 5 shows a macro image of the corroded Fe and FeMn samples, tested without magnetic field and with AC and DC after cleaning procedure. In pure Fe, different colors could be observed on the surface of the specimens because, although a dense layer of corrosion was not found, some products remained on it. The FeMn samples that were tested under magnetic fields, particularly DC, showed a considerable amount of reddish corrosion products (zone 5) adhered to their surface. In contrast, those tested without a magnetic field presented grey corrosion products (zone 1). In the center of FMDC-P a heterogenous distribution of small corrosion products were also found (zone 6). In the case of the AC condition, corrosion products were predominantly present at the border (point 4), whereas some small areas in the center of the sample were free of corrosion product (point 3).

Fig. 6 presents different surfaces of the degraded samples observed by SEM. The first noticeable feature was that while the FeH0-P shows some oxides on the surface, those degraded under magnetic field were almost free of corrosion products. Furthermore, two different topography patterns were revealed: grainy or lined (zones 1 and 2 in the micrograph, respectively). For FeH0-C, FeAC-C, and FeDC-C, the surfaces were mostly free from corrosion products and had a similar morphology to FeAC-P and FeDC-P, revealing grains (area 3). In addition, on FeDC-C, there were some areas (point 4) where the grains were not so easily detectable and a kind of squared pits were observed.

Fig. 7 shows SEM images of the corroded FeMn-P samples. The FMH0-P presented some small corrosion products (corresponding to point 1) forming plates similar in size to the grains. FeMn samples tested under the magnetic fields, both AC and DC, displayed spherical-shaped corrosion products (points 4 and 6) that were not present in FMH0-P, corresponding to the points 4 and 5 previously observed in the macro images in Fig. 5. Additionally, oxide-free areas were detected in the center of FMAC-P (point 3). In FMDC-P, apart from the spherical products at the borders of the sample, another morphology of corrosion products was also observed in the central area of the specimens, forming bigger plates than in the other conditions.

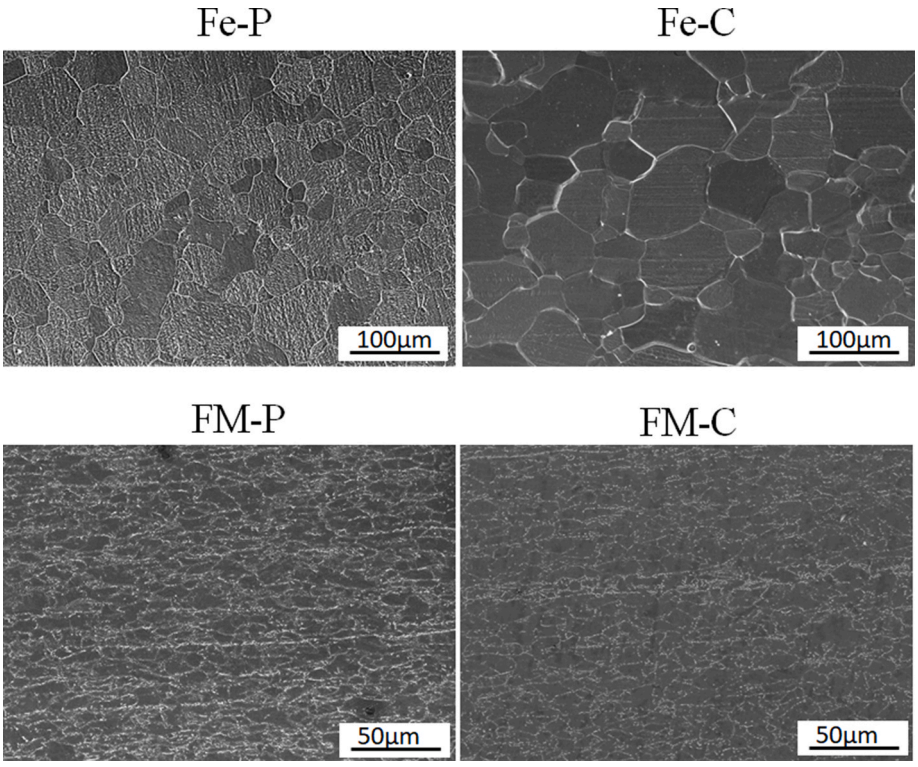

Fig. 3. Microstructure of as-received pure Fe and FeMn samples: Fe-P, Fe-C, FM-P and FM-C.

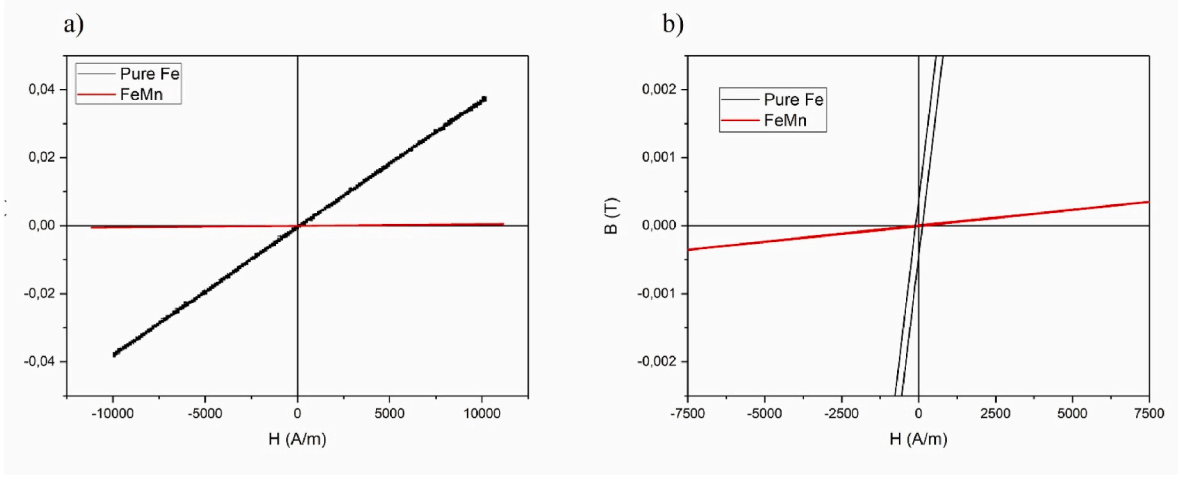

Fig. 4. Hysteresis loop of a) comparative ferromagnetic pure Fe and paramagnetic FeMn samples (7x14 × 1mm) and b) expanded graph of the hysteresis cycle of FeMn.

FMH0-C and FMAC-C exhibited a similar behavior than FMH0-P and FMAC-P. Small corrosion products were found in FMH0-C, identified as previously observed in point 1 in the macro images (Fig. 5) and in the micrograph of FMH0-P. For FMAC-C, spherical-shaped corrosion products appeared again (point 4) and the revealed grains were observed in the background (point 3). In the case of FMDC-C the grains were revealed, and neither plates nor spherical-shaped corrosion products were found.

3.4. Cross section

The thickness of the degradation product layer, that remained attached to the surface even after the mechanical cleaning procedure, was measured and compared for different conditions (Fig. 8). In FeH0 a maximum thickness of 86 µm was detected, corresponding to isolated cracked oxide particles observed in Fig. 6. The oxide layer had a mean thickness of 60.6 ± 19.1 µm showing a marked thickness inhomogeneity. On the contrary, FeAC showed a very thin corrosion layer (4.8 ± 0.5 µm), that was present only on some surface zones. No degradation products were detected on FeDC samples.

Regarding FeMn, FMH0 showed a non-uniform and thick corrosion layer (48.3 ± 7.4 µm), compared to the other degradation conditions. The layer was not compact but formed by loosely attached scales. FMAC showed a more uniform and thinner corrosion layer with an average thickness of 33.2 ± 2.7 µm. FMDC presented the thinnest degradation product layer (19.2 ± 3.8 µm), with transversal cracks reaching the substrate.

In general, it can be said that FeMn surfaces were covered by thicker

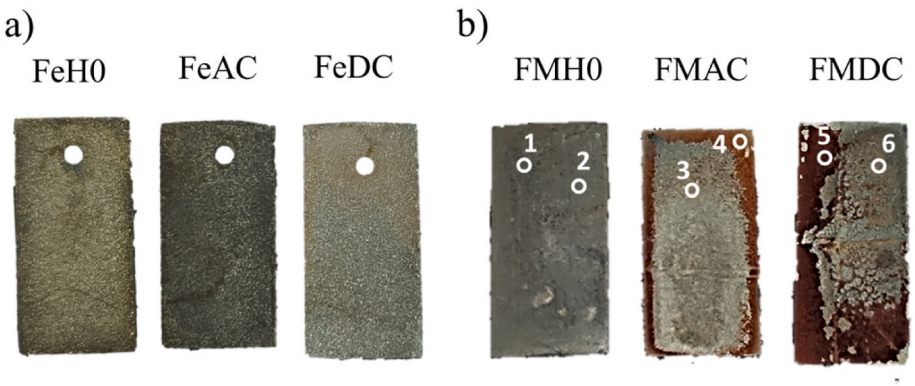

Fig. 5. Macro images after 14 days immersion in Hanks' solution and mechanical cleaning: a) FeH0-P, FeAC-P, FeDC-P and b) FMH0-P, FMAC-P, FMDC-P.

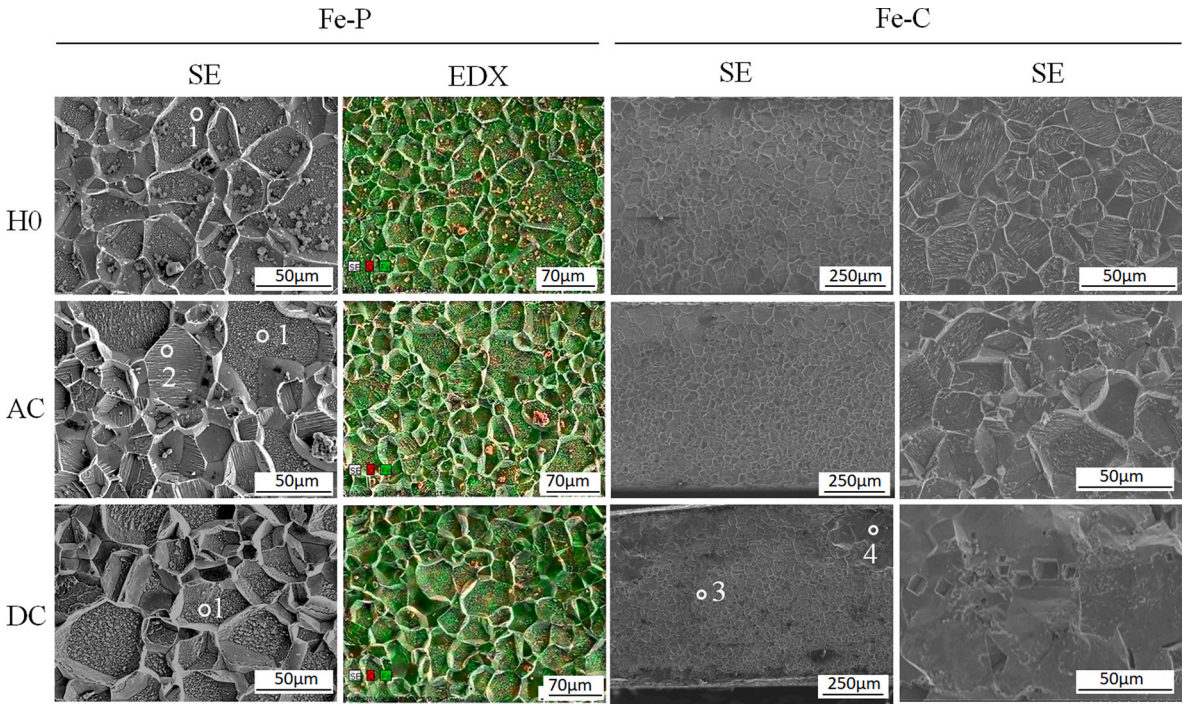

Fig. 6. SEM sample after 14 days immersion in Hanks' solution and mechanical cleaning of Fe-P (by column: SE and EDX, green corresponds to Fe and red to O) and Fe-C (by column: SE and SE at higher magnification).

corrosion product layers than Fe surfaces under the same condition, and that AC gave rise to thicker corrosion layers than DC.

3.5. XPS analysis

The compounds present in Fe-P and FeMn-P after the tests were analyzed by XPS and the results are represented in Figs. 9 and 10. Fig. 9 displays the atomic elemental composition. The elements observed on all the samples were C, O, Mg, Cl, and P, and Fe.Mn was detected on the Fe-Mn-based alloy. For pure Fe, the main element present was C, whose concentration was in the range of $C_C = \sim 55$ at. % for FeAC to $C_C = \sim 68$ at. % for FeDC. The amount of O was in the range of 8–30 at. % for FeDC and FeAC, respectively. A consistent amount of Mg ($C_{Mg} = \sim 10$ at. %) was found for FeDC and for FeAC, while Fe was present for all the conditions with a concentration of $C_{Fe} < \sim 5$ at. %. Traces of Cl and P were also detected. Elements like Mg, P, and Cl were found; they were compatible with the presence of phosphate and chloride anions from the solution salts, forming residual degradation products on the specimen surfaces. The amount of Cl and P found was very low. Cl was attributed to the presence of chlorides in the used salt and P to the phosphates ($PO_4^{3-}/HPO_4^{2-}/H_2PO_4^-$). For the FeMn system, C was present with a concentration in the range of ~55 (for FeDC) to ~68 at. % (for FeH0). The amount of O was in the range of 8–30 at. %, for FeDC and for FeAC respectively. Also in this case, a small amount of Fe and Mn was found, as well as traces of P and Cl.

The high-resolution spectra of C1s, O1s, and Fe2p were analyzed for pure Fe. Additionally, Mn2p was analyzed for FeMn. The fitting parameters for all peaks were included as Supplementary Material. Table S1 contains the parameters for Fe and Table S2 contains the parameters for FeMn. The O1s spectra for Fe-H0 were fitted with three peaks. The first peak at 529.9 eV (~30 % area) was attributed to the O bound to metal, forming a metal oxide (MO_x), related to the presence of different oxide phases (for example Fe_3O_4) [55]. The second peak located at 531.6 eV (~60 % of the whole peak area) was associated to Fe (III) oxy-hydroxides FeOOH [56], and the third peak marked at 533.3 eV (~10 % of the whole band area) was attributed to loosely bound adsorbed water [57]. The O1s FeAC and FeDC spectra showed the same band composition. The peaks found for the deconvolution of Fe2p3

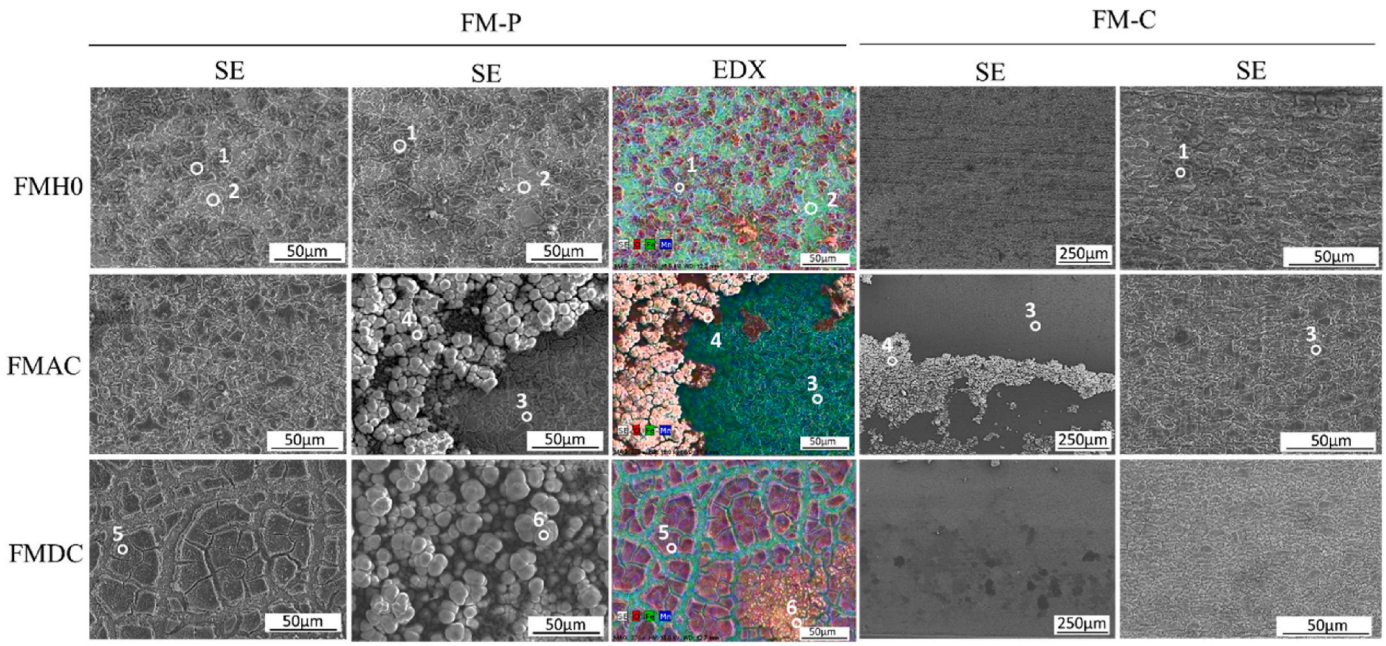

Fig. 7. SEM sample after 14 days immersion in Hanks' solution and mechanical cleaning of FM-P (by column: SE and EDX, green corresponds to Fe and red to O) and FM-C (SE).

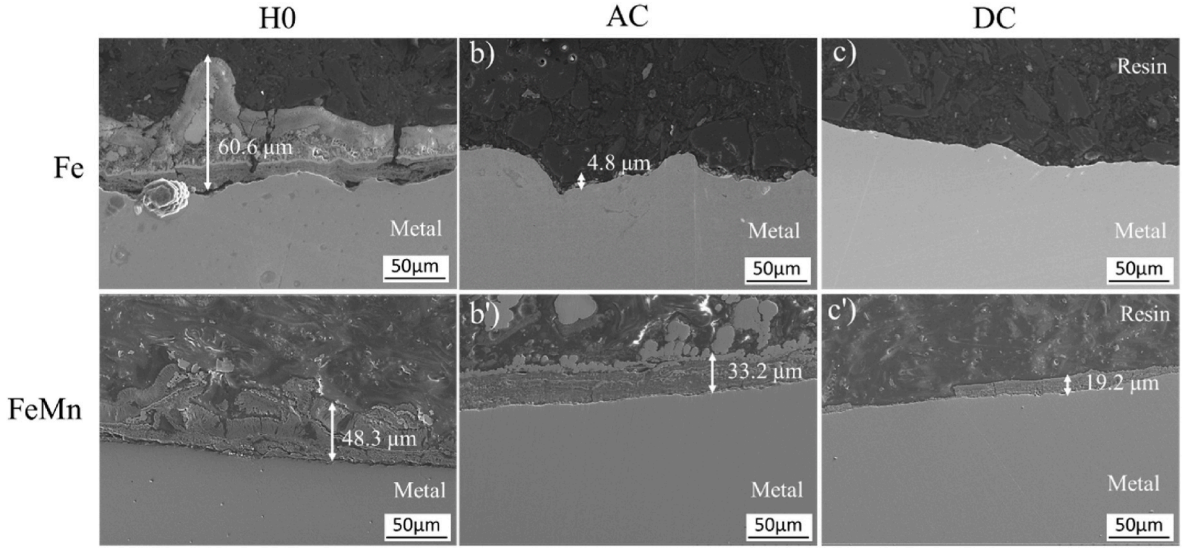

Fig. 8. SEM–SE sample cross-section micrographs after 14 days of immersion in Hanks' solution of Fe and FeMn.

showed the presence of Fe in both the two most common oxidized states, that is both Fe^{2+} and Fe^{3+}. The first peak situated at 707.3 eV (~5 % of the total peak area) could be related to Fe in its metallic shape [55]. The peak located about ~709.2 eV (~20 % of the whole peak area) was associated with magnetite (Fe_3O_4) and the rest of the peaks found during the deconvolution of Fe were attributed to Fe^{2+} and Fe^{3+} present in Fe_3O_4, and Fe^{3+} present in FeOOH [55,56].

Similar trends were found for all the conditions of the Fe-Mn alloy. The spectra of Mn2p3 curves fitted with multiple peaks, were attributed respectively to Mn(0) (639.5 eV [58]), and various Mn oxides (Mn_2O_3, MnO_2, Mn_3O_4, etc. for the peaks from 641 to 643 eV [59].

3.6. Corrosion products

The corrosion products were analyzed by FTIR and XRD (Fig. 11). For pure Fe the PO_4^{3-} band was observed at 1022 cm^{-1} and associated to the asymmetric stretching of the v3 group. Additionally, a low-intensity CO_3^{2-} absorption peak vibration at around 1637 cm^{-1} was present. The CO_3^{2-} bands at 1440 and 1216 cm^{-1} were detected only for the FeDC condition. The peak at 2932 cm^{-1}, with a shoulder at 2848 cm^{-1}, was assigned to OH^- stretching, and it was only found for FeAC and FeDC [60]. The broad peak at 3400 cm^{-1} was assigned to absorbed H_2O. In the case of removed products, they are similar to the detached products, presenting the PO_4^{-3} band at 1016 cm^{-1} and the CO_3^{2-} band at 1400 cm^{-1} and 1620 cm^{-1} [60–62].

For FeMn, the detached products exhibited a broad peak around 1060 cm^{-1} and three sharp vibration peaks were visible at around 527 cm^{-1}, 590 cm^{-1} and 620 cm^{-1}, corresponding to the PO_4^{-3} group. These three vibration peaks were less intense in FMH0 than in FMAC and FMDC. The CO_3^{2-} band at 1460 cm^{-1}, 1216 cm^{-1}, 880 cm^{-1}, and 770 cm^{-1} was detected, and the peak at 1647 cm^{-1} can be assigned to OH^- stretching vibrations [60]. Weak absorption bands in the region 2998

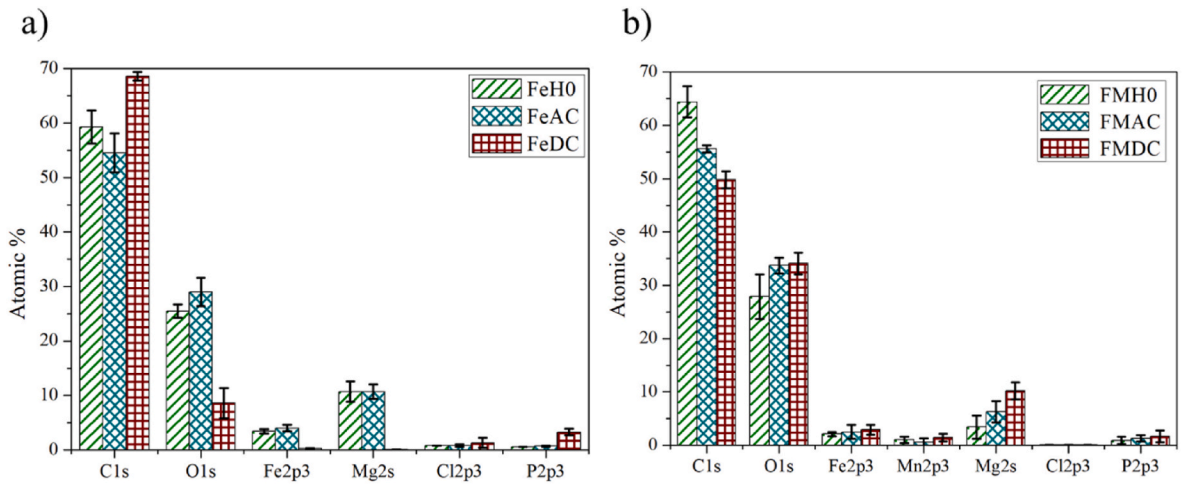

Fig. 9. XPS atomic percent of a) pure Fe and b) FeMn degraded samples.

cm^{-1} to 2883 cm^{-1} could be attributed to asymmetric or symmetric vibration bands of methylene (-CH_2), from organic ligands due to the presence of D-glucose in the solution [63]. For the removed products, a broad peak was visible at 1016 cm^{-1} corresponding to PO_4^{-3} group. A weak absorption band was found at 1383 cm^{-1} and attributed to CO_3^{2-} band. The peak at 1633 cm^{-1} was assigned to carboxyl groups [63]. The broad peak at 3400 cm^{-1} was again attributed to absorbed H_2O, and specifically both to the detached products and to the removed ones.

In the XRD analysis, independently from the magnetic field condition, the presence of three compounds were identified in the degradation products: lepidocrocite (γ-FeOOH), goethite (α-FeOOH) and magnetite (Fe_3O_4). In the FeMn spectra two different compounds were found: iron oxide (ε−Fe_2O_3) and goethite (α-FeOOH).

3.7. Corrosion rate

The results of mass loss and corresponding corrosion rates are represented in Fig. 12. In the case of pure Fe, Fig. 12 a, the application of a magnetic field caused an increase in the corrosion rate from 0.101 ± 0.007 mm/year (FeH0) to 0.181 ± 0.004 mm/year for FeAC, and to 0.204 ± 0.001 mm/year for FeDC. This implied that the corrosion rate was roughly doubled by the application of a 6500 A/m magnetic field, either AC or DC. It is to be highlighted the low standard deviation of these results.

In the case of FeMn (Fig. 12b), the corrosion rates obtained were 0.130 ± 0.065 mm/year for FMH0, 0.114 ± 0.026 mm/year for FMAC, and 0.135 ± 0.063 mm/year for FMDC. From these values, and the graphical representation, it was evident that in this alloy the standard deviations were too high to allow for a discrimination between its behavior with and without a magnetic field. Upon closer analysis, it appeared that a significant amount of corrosion products remained attached to the alloy surface, leading to a misestimation of the actual mass loss.

To calculate the corrosion rate of FeMn alloys, an alternative method was employed to obtain the mass loss. This method was based on the measurement of the loss of thickness of the samples, as shown in Fig. 12 c. The results of thickness loss are shown in Fig. 12 d, where it can be seen that FMDC has higher thickness than FMH0 and FMAC. To determine whether the differences between FMDC and the other two conditions were significant, a statistical analysis using ANOVA and Tukey's test was conducted (Fig. S1 in the Supplementary Material). Based on this analysis, it could be concluded that the thickness loss of FMDC was significantly higher than those of FMH0 and FMAC (p-value <0.05 was considered statistically significant). The results of mass loss and CR, as indirectly obtained from thickness loss measurements, were represented in Fig. 12 e, where it could be seen that FMDC had a higher mean CR (0.960 ± 0.422 mm/year) than FMH0 and FMAC (0.367 ± 0.193 and 0.485 ± 0.213 mm/year, for FMH0 and FMAC, respectively), indicating that, for the FeMn alloy, the application of a 6500 A/m direct magnetic field significantly increased its corrosion rate.

4. Discussion

The results presented above show that the application of a 6500 A/m magnetic field, either alternating or direct, increased about twice the CR of pure Fe in modified Hanks'solution, and that a direct magnetic field increased more than twice the CR of Fe12Mn1.2C in the same solution. Several authors have investigated the influence of a direct magnetic field in the corrosion behavior of metals, showing that it strongly depend on the anode material, pH media, magnetic field intensity and relative direction between the anode surface and the applied magnetic field. Moreover, it has been reported that magnetic fields can either decrease [40,64,65] or increase [66] the corrosion rates of metals. With regard to Fe, Lu and Chen studied the effect of the field in a neutral sodium sulfate solution and demonstrated with potentiodynamic tests that a 0.4 T (318 kA/m) flux density parallel to the Fe anode surface produces an enhancement of the current density of the corrosion process and a narrowing of the passive potential range, which corresponds to a higher corrosion rate and a more unstable oxide layer [67]. However, no studies are available so far in relation to the effect of magnetic field on the corrosion of metals in simulated body fluids. In addition, one recent potentiodynamic study about Fe and an Fe-Ga alloy in simulated body fluid under a direct 60 mT-field reported that corrosion rate doubles under the action of the magnetic field [44]. However, no studies are available in relation to the effect of magnetic field on the corrosion of Fe and Fe-Mn alloys in Hanks' solution at 37 °C.

The differences between the materials when a magnetic field is applied requires a deep analysis of the actual distribution of the magnetic flux density in the samples. According to the literature, the main effect of direct magnetic fields on electrochemical processes is the modification of mass transport due to the Lorentz force (eq. (2)), which accelerates the moving charges in the direction perpendicular to the current and flux density:

$$\vec{F}_L = q\left(\vec{v} \times \vec{B}\right) \tag{2}$$

where q and v are the electrical charge (A·s, or C) and velocity (m/s) of the moving particle and B is the magnetic flux density (T). The field acts as a gentle stirring that can modify the features of the diffusion layer, such as its thickness or the concentration of chemical species within it

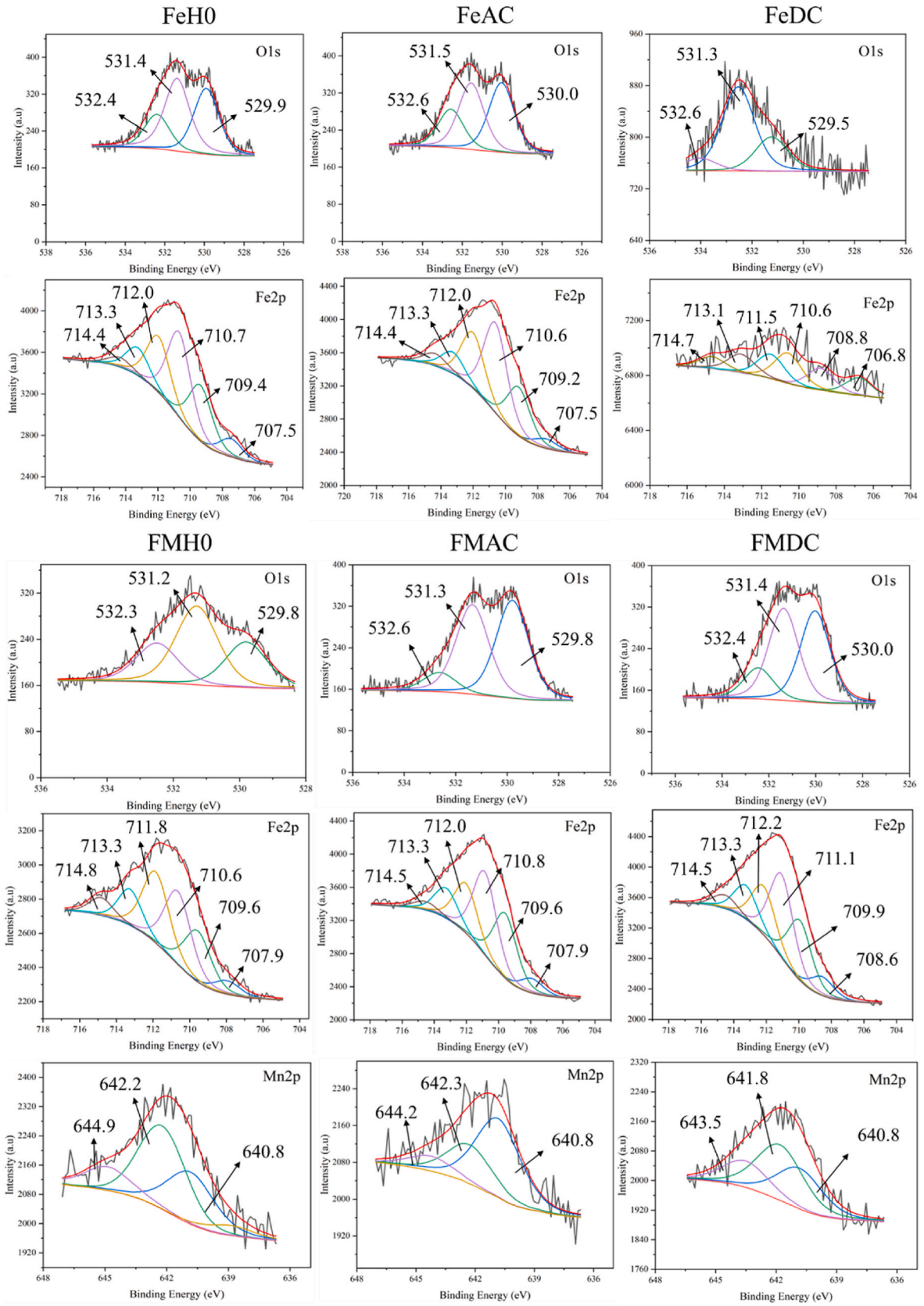

Fig. 10. High resolution XPS spectra of O1s and Fe2p in Fe-P samples and O1s, Fe2p and Mn2p in FM-P samples for magnetic conditions H0, AC and DC.

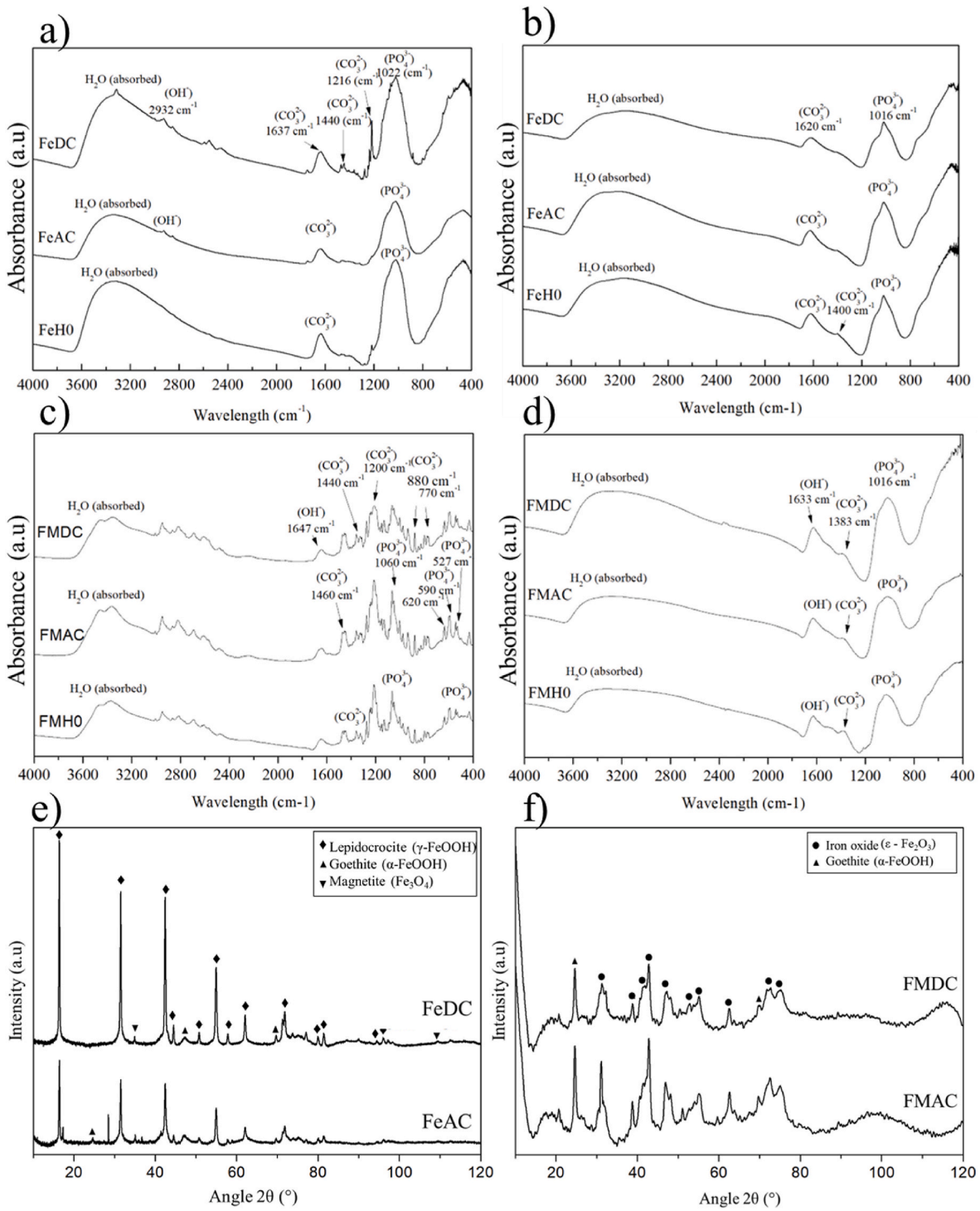

Fig. 11. Results from the corrosion product analysis: FTIR on detached and removed corrosion products after 14 days of immersion: a-b) pure Fe and c-d) FeMn, respectively and e-f) XRD analysis of removed products of Fe and FeMn samples.

[68]. This is called the magnetohydrodynamic (MHD) effect. In addition, when the field is non-uniform, a force due to the flux density gradient (∇B) can also arise [68]. This flux density gradient force can move paramagnetic particles, as Fe^{2+} ions, into areas of high magnetic flux density. In the specific case of ferromagnetic anodes, Sueptitz et al. [39] claimed that under certain conditions the field gradient force can overcome the effect of the Lorentz force.

In the case of an alternating magnetic field, in addition to the alternating Lorentz force, electric currents are induced in the surface of the metallic specimens, as Faraday's law of induction predicts.

Fig. 13a-c shows the numerically simulated magnetic flux density distribution in the space close to Fe and FeMn specimens, and Fig. 13e-g represents the distribution of B across the width of the samples, for an alternating applied field of 6500 A/m peak amplitude and a direct applied field of 6500 A/m.

In the case of FeAC (Fig. 13a), the induced currents limit the penetration of the magnetic field to the surface of the sample [69]. In Fig. 13 e B magnitude is represented across the width of the sample in a plane at the middle and at the top extreme of the specimens. It is appreciated that B reaches the highest values (~0.56 T) at the rim of the center of the

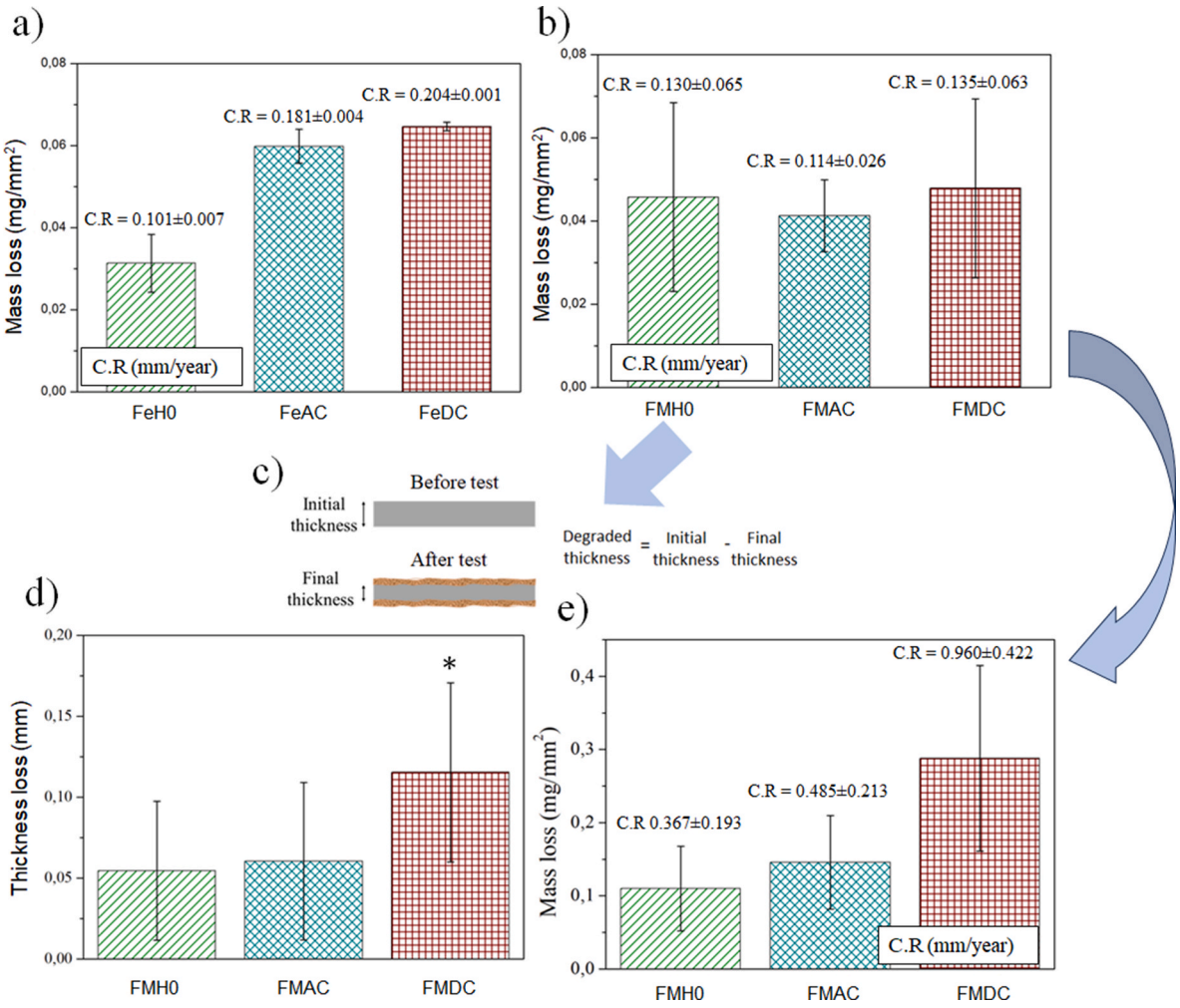

Fig. 12. a-b) Mass loss (mg/mm^2) and corrosion rate (mm/year) for pure Fe and FeMn samples obtained by weight loss; c) dimensional metrology process; d) thickness loss. *p < 0.05 compared to FMH0 and FMAC; and e) mass loss (mg/mm$_2$) and corrosion rate (mm/year) of FeMn samples derived from thickness loss measurement.

sample (Fig. 13h) causing $\nabla B \sim 22$ T/mm in the area surrounding the specimen surface. On the contrary, FeDC has a more uniform distribution within the sample and lower value of flux density (~0.03 T, in good agreement with the experimental value shown in Fig. 4) than FeAC, leading to ∇B ~1 T/mm. The fact that the CR value is similar for both conditions, despite the fact that ∇B is one order of magnitude higher for FeAC could suggests that the Lorentz force has greater relevance than the flux density gradient force in the specific studied electrochemical process. Further potentiodynamic experiments are in progress to assess the role that the different magnetic forces play under a 6500 A/m field in modified Hanks' solution.

For FeMn samples, the same magnetic field distribution was obtained for AC and DC, so only the results of AC simulation are depicted (Fig. 13c and Fig. 13g). As expected for a paramagnetic material, the value of B is lower than for a ferromagnetic one and causes a small deviation of flux lines [70], and therefore an also small ∇B (~0,1 T/mm). This suggests, as in the case of Fe, that under these experimental conditions the Lorentz force has greater relevance. Actually, these forces have been studied by many researchers [39,66,70,71]. Specifically, Grant et al. observed that the field gradient force may become significant in non-uniform magnetic fields when a field gradient is deliberately imposed ($\nabla B \gg 1$ T/m) [72,73]. In addition, although the intensity and distribution of B is the same for both cases, the higher average corrosion rate obtained by thickness loss measurements for FMDC could suggest that the stirring effect of the direct field was more effective than the 50 Hz alternating one.

Therefore, the observed rise of the corrosion rate could be associated to the movement of ions under the magnetic field produced by the previously mentioned Lorentz force. For a charged particle (cation, anion, etc.) moving with a velocity not in the same direction as the magnetic field, the velocity component perpendicular to the magnetic field creates circular motion, whereas the component of the velocity parallel to the field makes the particle to move along a straight line, resulting in a helical motion [74] as represented in Fig. 14 a. This movement produces a stirring effect that increases the probability of the charges to reach the surface of the metal (Fig. 14b). Lioubashevsk et al. [75] proposed a theoretical hydrodynamic model describing how Lorentz force acts on planar electrode surfaces and they discovered that the introduction of a magnetic field can decrease the thickness of the diffusion boundary layer, and that the reduced thickness results in an enhanced supply of active species increasing the mass transfer limited current.

As already mentioned in the introduction, many studies have been conducted to increase the corrosion rate of iron using different strategies. The results of some of these studies are summarized in Table 2. Oriňaková et al. examined the impact of polyethylene glycol (PEG) coating on the microstructure and corrosion properties of open-cell iron foams and phosphorus/iron foams, observing that PEG coating resulted in an increase in corrosion rates in both foams [76]. On the other hand, Liu et al. employed alloying techniques to enhance the degradation of pure iron. They used various elements (Mn, Co, Al, W, B, C, and S) as

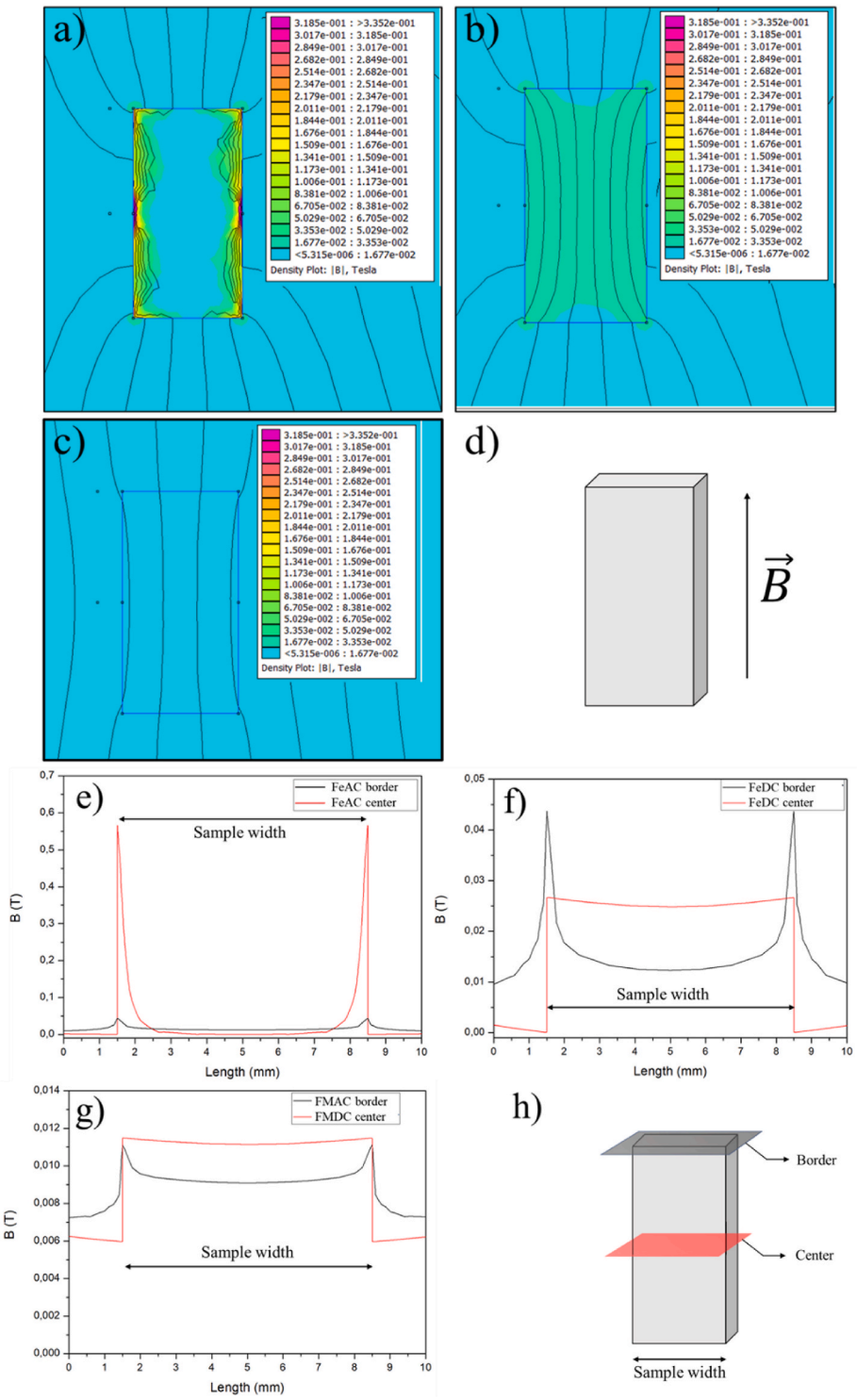

Fig. 13. Magnetic field simulation of Fe and FM samples: a)-c) flux density distribution (B); d) scheme of the applied B direction with respect to the sample; e)-g) flux density across the width of the specimens; g) scheme of the crosslines represented in e)- g).

alloying agents and found that, except for the Fe-Mn alloy which showed a decrease in the degradation rate, the degradation rates of the remaining Fe-X binary alloys were similar to that of pure iron [7]. Huang et al. used metal vapor vacuum arc technology to implant zinc ions into the surface of pure iron, observing an increase in the corrosion rate of Fe after the implantation of Zn ions [77]. Moravej et al. observed that electroformed iron showed faster degradation than cast iron with a uniform degradation mechanism [30]. Qi et al. investigated the use of metal-polymer stents employing a PLA coating on Fe stents. They observed an acceleration of the coated stent attributed to the relatively lower local pH produced by PLA hydrolysis, achieving a corrosion rate of 0.088 mm/year [78].

Table 3 summarises the corrosion rate obtained by other authors for FeMn alloys. Mouzou et al. investigated the corrosion behavior of the Fe20Mn1.2C alloy in different solutions, obtaining that the CR was higher in commercial Hank's solution (0.165 mm/year) than in modified Hank's solution (0.115 mm/year). They attributed this difference in CR to the formation of an insoluble $MnCO_3$ layer, which may hinder

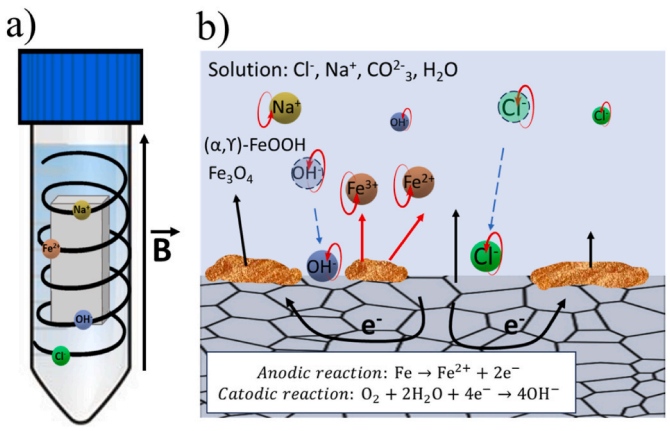

Fig. 14. Diagram of the behavior of charges in the presence of magnetic fields: a) movement of charges in the presence of DC; b) scheme of the corrosion process.

Table 2
Corrosion rates (CR) measured by weight loss collected from the literature for Fe.

Material	Test	Solution	C.R (mm/year)	Ref
Fe	Static immersion	Hank's	0.0231	[76]
Fe-PEG			0.0455	
Fe/P			0.0131	
Fe/P-PEG			0.0397	
Fe cast	Static immersion	Hank's	0.0118	[7]
Fe rolled			0.0077	
Fe-Mn cast			0.0017	
Fe-Mn rolled			0.0013	
Fe-Co cast			0.0116	
Fe-Co rolled			0.0102	
Fe-Al cast			0.0065	
Fe-Al rolled			0.0054	
Fe	Static immersion	Hank's	0.0222	[77]
	Electrochemical		0.0273	
Fe with ions Zn	Static immersion		0.0278	
	Electrochemical		0.0986	
Fe electroformed	Static immersion	Hank's	0.40	[30]
Fe electroformed and annealing			0.25	
Fe-PLA coated	In vivo		0.088	[78]

further metal dissolution [79]. Hermawan et al. conducted degradation tests on Fe(20-35Mn) alloys, with quenched and rolled parts, obtaining a range of CR between 0.4 and 1.3 mm/year [33]. Gambaro et al. [45] investigated the effect of different Mn and C contents on phase formation and CR in a modified Hank's solution. For the alloy with the same composition used in this study, Fe12Mn1.2C, they obtained a CR of 0.148 mm/year, in the range of that obtained in the present study also by the weight loss method (0.130 mm/year), but clearly inferior to that obtained by the thickness method (0.367 mm/year), Fig. 12. Given that those authors reported the presence of corrosion products adhered to the surface of the samples after washing, it could be assumed that their measurements may underestimate the actual mass loss, and that a measurement through the thickness loss offers more realistic results for samples where corrosion products remain partially or totally attached.

While many authors have researched and successfully increased the degradation rate of Fe-based materials, the proposal of the present research aims not only to accelerate the degradation rate of ferrous implants, but also to be able to modify it in a non-invasive way according to the patient's needs once the prosthesis has been implanted.

Table 3
Corrosion rate (C.R) results collected from the literature for FeMn alloys.

Material	Test	Solution	C.R (mm/year)	Ref
Fe20Mn1.2C	Static immersion	Hank's	0.165	[79]
Fe20Mn1.2C		Hank's modified	0.115	
Fe20Mn TT	Potentiodynamic polarization	Hank's modified	1.3	[33]
Fe20Mn cold rolled			0.5	
Fe25Mn TT			1.1	
Fe25Mn cold rolled			0.5	
Fe30Mn TT			0.7	
Fe30Mn cold rolled			0.7	
Fe35Mn TT			0.4	
Fe35Mn cold rolled			0.7	
Fe12Mn1.2C	Static immersion	Hank's modified	0.148	[45]
Fe16Mn0.9C			0.155	
Fe20Mn0.6C			0.134	

Regarding the corrosion products, it is important to mention that the use of magnetic fields did not significantly modify the chemical composition of the corrosion products of Fe and FeMn after 14 days of immersion in modified Hanks' solution. T. Peev studied the influence of magnetic fields on chemical and electrochemical processes on steel in different media (mine water, industrial waste H_2S-containing water, sea water, 3 % NaCl solution). They observed some changes in the corrosion processes mechanism, leading to the elimination of some stages or the creation of others, promoting the formation of some corrosion products depending on the corrosive medium [80]. According to the literature, the degradation of iron in a physiological environment can be expressed by the reactions (eq. 3-eq. (7)) [81]:

$$Anodic\ reaction: Fe \rightarrow Fe^{2+} + 2e^{-} \quad (3)$$

$$Catodic\ reaction: O_2 + 2H_2O + 4e^{-} \rightarrow 4OH^{-} \quad (4)$$

$$Fe^{2+} + 2OH^{-} \rightarrow Fe(OH)_2 \quad (5)$$

$$Fe^{2+} \rightarrow Fe^{3+} + e^{-} \quad (6)$$

$$Fe^{3+} + 3OH^{-} \rightarrow Fe(OH)_3 \quad (7)$$

In the presence of oxygen and chloride ions, $Fe(OH)_3$ is hydrolyzed and goethite (α-FeOOH) precipitates [82]. $Fe(OH)_2$ reacts with some of the FeO(OH), resulting in the formation of magnetite Fe_3O_4, a protective iron oxide layer, lowering the corrosion rate:

$$Fe(OH)_2 + 2FeO(OH) \rightarrow \boldsymbol{Fe_3O_4} + 2H_2O \quad (8)$$

Hank's solution is composed by phosphates, sulphates, chlorides and carbonates. During anodic oxidation, Fe^{2+} ions may be formed, facilitating the formation of iron phosphate. The proposed equilibrium equations are shown in the following equations [81]:

$$Fe(OH)_2 + Cl^{-} \rightarrow FeClOH + OH^{-} \quad (9)$$

$$FeClOH + H^{+} \rightarrow Fe^{2+} + Cl^{-} + H_2O \quad (10)$$

$$Fe^{2+} + O_2 + 3OH^{-} \rightarrow \boldsymbol{Fe(OH)_3}\downarrow + O^{2-} \quad (11)$$

$$Fe(OH)_3 + 2Cl^{-} \rightarrow FeCl_2OH + 2OH^{-} \quad (12)$$

$$FeCl_2OH + H^{+} \rightarrow Fe^{3+} + 2Cl^{-} + H_2O \quad (13)$$

$$6PO_4^{3-} + 10Ca^{2+} + 2OH^- \rightarrow \boldsymbol{Ca_{10}(PO_4)_6(OH)_2}\downarrow \quad (14)$$

$$3Fe^{2+} + 2PO_4^{3-} + 8H_2O \rightarrow Fe_3(PO_4)_2 8H_2O \quad (15)$$

$$PO_4^{3-} + Fe^{3+} \rightarrow \boldsymbol{FePO_4}\downarrow \quad (16)$$

$$CO_2(g) \leftrightarrow CO_2(aq) + H_2O \rightarrow H_2CO_3 \leftrightarrow H^+ + HCO_3^- \quad (17)$$

$$HCO_3^- \leftrightarrow CO_3^{2-} + H^+ \quad (18)$$

$$Fe^{2+} + CO_3^{2-} \leftrightarrow \boldsymbol{FeCO_3}\downarrow \quad (19)$$

$$FeO + O_2 \leftrightarrow \boldsymbol{2Fe_2O_3}\downarrow \quad (20)$$

The presence of Cl^- ions enhances the corrosion rate of Fe and passivation does not occur. They play a predominant role in the corrosion process compared with bicarbonate and carbonate ions. Degradation products do not cover the surface homogeneously, and chloride ions concentrate at preferential sites, hindering the formation of a passive layer. Water hydrolyses the metal chloride, forming hydroxide and free acids, and the corrosion product formed is predominantly γ-FeOOH [81]:

$$4Fe^{2+} + Cl^- + 8H_2O \rightarrow Fe_4(OH)_8Cl + 8H^+ + 9e^- \quad (21)$$

$$Fe_4(OH)_8Cl \rightarrow 4\boldsymbol{\gamma\text{-}FeOOH} + Cl^- + 4H^+ + 3e^- \quad (22)$$

The described reactions explain the formation of the corrosion products identified by XRD and XPS, which are similar to those previously reported for ferrous materials in modified Hanks' solution: lepidocrocite (γ-FeOOH), goethite (α-FeOOH) and magnetite (Fe_3O_4) and iron oxide (ε - Fe_2O_3) [47,81,83,84]. Tolouei et al. performed studies on the degradation behavior of pure Fe in multiple physiological solutions (NCS, CHBS, MHBS and DPBS) and found out that the principal degradation products were a mixture of magnetite, α-FeOOH and γ-FeOOH [85]. Huang et al. carried out static immersion tests in Hanks' solution for 30 days and the corrosion products were Fe_2O_3 and $Fe(OH)_2$ exhibiting good biocompatibility in cytotoxic tests [77]. Zang et al. and Dong et al. investigated the degradation of Fe for biomedical applications and detected $Ca_{10}(PO_4)_6(OH)_2$, $Ca_3(PO_4)_2$, $CaCO_3$, $FePO_4$ and $Fe_3(PO_4)\cdot 8H_2O$ [81,84]. For Fe20Mn1.2C, Mouzou et al. observed the presence of lepidocrocite (γ-FeOOH), goethite (α-FeOOH) and rhodochrosite ($MnCO_3$) by XRD.

In the present research, carbonates and phosphates were not detected, however, OH^-, PO_4^{3-} and CO_3^{2-} groups have been identified by FTIR in both Fe and FeMn. This suggests the presence of carbonates and phosphates cannot be discarded, so they may be either too small or amorphous.

It is important to note that some corrosion products are ferromagnetic, such as ε- Fe_2O_3 and Fe_3O_4 [85–87]. It cannot be discarded that the magnetic field may exert a force causing ferromagnetic corrosion products to move. However, no suspended particles were found in the test container, and corrosion products were indeed found deposited on the bottom of the container. Therefore, if magnetic forces were acting on the corrosion products, they would be significantly weaker than the force of gravity. If magnetic fields were to induce movement of ferromagnetic corrosion products, they could facilitate the detachment of the corrosion layer. This could be one of the reasons for achieving a higher corrosion rate in samples tested under magnetic fields. In the specific case of FeMn, it was observed that samples under magnetic fields exhibited more corrosion products adhered to the surface than FMH0, which may be an indication that the layer is not being detached as much by the magnetic fields.

Although no differences in the composition of the corrosion products were observed, in the case of FeMn, differences in their morphology were found between samples with and without a magnetic field (Fig. 7). In FMAC, spherical oxides are formed, which are not seen in FMH0, where only small plate-shaped products are seen. With regard to FMDC-P (the condition with the highest corrosion rate), two different morphologies were observed: spherical and large plate-shaped particles, indicating that the application of DC magnetic fields may favor the growth of the plates. The reason for this behavior may be a preferential orientation of oxides due to the direct magnetic field. In this line, Chen et al. [88] obtained textured BaM hexaferrite using rod-shaped α-FeOOH particles that were oriented by a direct magnetic field during sintering. Large plates are more prone to form cracks and suffer spallation, which lead to bare surface areas where the degradation process continues [51,52].

As noted above, no differences in the morphology of the corrosion products were observed in the Fe samples, but micrometric square pits were observed on the bare metal on FeDC-C. The corrosion tendency of pure Fe is strongest on the closely packed crystal faces (111) and (110), whereas grains with (100) orientation dissolve significantly slowly [91], resulting in the preferential dissolution of (001), (011) and (111) grains [48]. Fig. 15 shows the proposed mechanism of the square pitting corrosion. Pure iron is degraded by intergranular corrosion (yellow line in Fig. 15) and, as mentioned before, the corrosion progression is faster for grain orientations with closely packed crystal faces (111) and (110), while grains with (100) orientation dissolve much slowly. This retraction (blue line in Fig. 15) would result in the square pits detected in the SEM image (Fig. 6) [89,90,92,93]. Nevertheless, these square pits were only clearly detected in FeDC-C samples, therefore the effect of magnetic domains, or another magnetic feature, cannot be discarded. Further studies should be done for clarifying their origin. It is worthy noticing that despite the appearance of those squared formations, not signals of pitting corrosion have been detected.

Despite the different magnetic properties shown by pure Fe and FeMn alloy, it has been proved that when exposed to a magnetic field the corrosion rate of both Fe-based materials is accelerated. For each material, although the morphology of their corrosion products with and without a magnetic field presents some dissimilarities, their chemical compositions remain the same. Therefore, it is reasonable to assume that their biocompatibility will not change because of the field. Consequently, it can be hypothesized that magnetic fields could potentially be used as an adjuvant to stimulate the biodegradation of ferrous cardiovascular stents.

The next step in this investigation would be to explore the effectiveness of intermittent exposure to magnetic fields on the degradation rate of a ferrous implant. By intermittent it is meant, for example, for 1 h a day. This would assimilate the procedure to, for example, the well-established one for rehabilitation and physiotherapy practice or to those proposed as alternative treatments against biofilms in metallic implants [94–96].

It is worth noticing that the intensity of the magnetic field applied in our experiments (6.5 kA/m = 8.2 mT) is within the low range of those

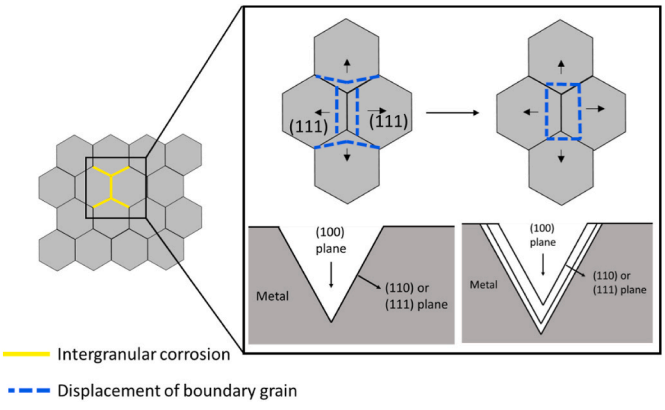

Fig. 15. Proposed mechanism for the square pitting formation.

used in physiotherapy (3–100 mT) [96]. Therefore, there is still a broad range of field intensities to be explored, which in combination with intermittent exposures might lead to the optimization of a procedure to accelerate the degradation rate of ferrous stents.

5. Conclusions

The assessment of the effect of magnetic field on the corrosion rate of pure Fe and Fe12Mn1.2C were performed by 14-day static immersion corrosion tests in modified Hanks' solution, using both alternating and direct magnetic fields with 6500 A/m of intensity.

The CR of Fe under magnetic field doubles the CR values without field, and the CR of Fe12Mn1.2C is almost three times higher with field than without. Due to the relatively high amount of corrosion products that remain attached to the Fe12Mn1.2C surface, its CR was evaluated by two procedures, mass loss and thickness loss measurements, resulting the latter more reliable to calculate its CR. The homogeneous corrosion generally developed by the studied materials was not altered by the application of the magnetic fields.

Regarding the composition of the corrosion products, no effect of the magnetic fields was detected. However, the size of the plate-shaped aggregates that remain on the surface of Fe12Mn1.2C tested with DC magnetic field was larger than those formed under the other conditions.

The fact that, under certain conditions, the application of magnetic fields increases the corrosion rate of Fe and Fe12Mn1.2C, and that the corrosion proceeds in a homogeneous way with similar chemical composition of corrosion products encourage the continuation of research in this area.

Ethics approval and consent to participate

The study reported in manuscript entitled "*Study of the effect of magnetic fields on static degradation of Fe and Fe-12Mn-1.2C in balanced salts modified Hanks' solution*" by I. Limón, M. Multigner and co-authors does not involved animals studies, the use of any animal or human data, therefore the section "Ethics approval and consent to participate" is "Not applicable".

CRediT authorship contribution statement

Irene Limón: Writing – original draft, Visualization, Investigation. **Marta Multigner:** Writing – original draft, Visualization, Project administration, Investigation, Funding acquisition, Conceptualization. **Carlo Paternoster:** Writing – review & editing, Supervision, Investigation, Conceptualization. **Marcela Lieblich:** Writing – review & editing, Supervision, Funding acquisition. **Belén Torres:** Writing – review & editing, Supervision, Project administration, Funding acquisition. **Diego Mantovani:** Writing – review & editing, Supervision, Resources, Project administration, Funding acquisition. **Joaquín Rams:** Writing – review & editing, Supervision, Resources, Project administration, Funding acquisition.

Declaration of competing interest

D.M is an associate editor for *Bioactive Materials* and was not involved in the editorial review or the decision to publish this article. All authors declare that there are no competing interests.

Acknowledgments

Financial support of Ministry of Science and Innovation of Spain (MICINN) PID2021-123891OB-I00. PID2021-124341OB-C21 and PID2022-139323NB-I00 funded by MCIN/AEI/10.13039/501100011033. Rey Juan Carlos University, Móstoles (Madrid) Spain has funded the C1PREDOC2020 grant of Irene Limón. This work was partially supported by the Natural Science and Engineering Research Council of Canada, the Fonds de la Recherche du Québec sur les Natures et les Technologies, and the Canada Foundation for Innovation.

Appendix ASupplementary data

Supplementary data to this article can be found online at https://doi.org/10.1016/j.bioactmat.2024.06.027.

References

[1] Canadian Agency for Drugs and Technologies in Health, Bioabsorbable Stents for Adults with Coronary Artery Disease: A Review of the Clinical Effectiveness, Cost-Effectiveness, and Guidelines, CADTH: Rapid Response Report, no. December, 2013, pp. 1–14 [Online]. Available: https://www.ncbi.nlm.nih.gov/books/NBK195783/.

[2] W. Herrington, B. Lacey, P. Sherliker, J. Armitage, S. Lewington, Epidemiology of atherosclerosis and the potential to reduce the global burden of atherothrombotic disease, Circ. Res. 118 (4) (Feb. 2016) 535–546, https://doi.org/10.1161/CIRCRESAHA.115.307611.

[3] J. Goldman, J.W. Drelich, Biodegradable metals for cardiovascular stents: from clinical concerns to recent Zn - alloys, Adv. Healthcare Mater. 5 (10) (2017) 1121–1140, https://doi.org/10.1002/adhm.201501019.Biodegradable.

[4] L.J. Laslett, et al., The worldwide environment of cardiovascular disease: prevalence, diagnosis, therapy, and policy issues: a report from the american college of cardiology, J. Am. Coll. Cardiol. 60 (25 SUPPL) (2012), https://doi.org/10.1016/j.jacc.2012.11.002.

[5] M. Moravej, D. Mantovani, Biodegradable metals for cardiovascular stent application: interests and new opportunities, Int. J. Mol. Sci. 12 (7) (2011) 4250–4270, https://doi.org/10.3390/ijms12074250.

[6] M. Schinhammer, I. Gerber, A.C. Hänzi, P.J. Uggowitzer, On the cytocompatibility of biodegradable Fe-based alloys, Mater. Sci. Eng. C 33 (2) (2013) 782–789, https://doi.org/10.1016/j.msec.2012.11.002.

[7] B. Liu, Y.F. Zheng, Effects of alloying elements (Mn, Co, Al, W, Sn, B, C and S) on biodegradability and in vitro biocompatibility of pure iron, Acta Biomater. 7 (3) (2011) 1407–1420, https://doi.org/10.1016/j.actbio.2010.11.001.

[8] Coronary stent market size and trends report, 2023-2030. https://www.strategicmarketresearch.com/market-report/coronary-stents-market, 2024 April.

[9] Bioabsorbable Stents Market – Global Industry Analysis and Forecast (2023-2029)." https://www.maximizemarketresearch.com/market-report/global-bioabsorbable-stents-market/21634/].

[10] T. Muramatsu, et al., Avances en el tratamiento mediante intervención coronaria percutánea: el stent del futuro, Rev. Esp. Cardiol. 66 (6) (2013) 483–496, https://doi.org/10.1016/j.recesp.2012.12.009.

[11] Y. Blake, Biocompatible materials for cardiovascular stents, Zenodo 1 (December) (2020) 1–9, https://doi.org/10.5281/zenodo.4321792.

[12] G. Gabriela, Biodegradable iron-based materials — what was done and what more can Be done, Materials 14 (13) (2021) 3381, https://doi.org/10.3390/ma14123381.

[13] P. Zartner, M. Buettner, H. Singer, M. Sigler, First biodegradable metal stent in a child with congenital heart disease: evaluation of macro and histopathology, Cathet. Cardiovasc. Interv. 69 (3) (Feb. 2007) 443–446, https://doi.org/10.1002/ccd.20828.

[14] P. Zartner, R. Cesnjevar, H. Singer, M. Weyand, First successful implantation of a biodegradable metal stent into the left pulmonary artery of a preterm baby, Cathet. Cardiovasc. Interv. 66 (4) (Dec. 2005) 590–594, https://doi.org/10.1002/ccd.20520.

[15] D. Schranz, P. Zartner, I. Michel-Behnke, H. Akintürk, Bioabsorbable metal stents for percutaneous treatment of critical recoarctation of the aorta in a newborn, Cathet. Cardiovasc. Interv. 67 (5) (May 2006) 671–673, https://doi.org/10.1002/ccd.20756.

[16] Y.F. Zheng, X.N. Gu, F. Witte, Biodegradable metals, Mater. Sci. Eng. R Rep. 77 (Mar. 2014) 1–34, https://doi.org/10.1016/j.mser.2014.01.001.

[17] A.L. Ramirez–Ledesma, et al., Microstructural precipitation evolution and in vitro degradation behavior of a novel chill-cast Zn-based absorbable alloy for medical applications, Metals 10 (5) (Apr. 2020) 586, https://doi.org/10.3390/met10050586.

[18] A.L. Ramirez–Ledesma, L.A. Domínguez–Contreras, J.A. Juarez–Islas, C. Paternoster, D. Mantovani, Influence of cross – rolling on the microstructure and mechanical properties of Zn bioabsorbable alloys, Mater. Lett. 279 (Nov. 2020) 128504, https://doi.org/10.1016/j.matlet.2020.128504.

[19] H.S. Han, S. Loffredo, I. Jun, J. Edwards, Y.C. Kim, H.K. Seok, F. Witte, D. Mantovani, S. Glyn-Jones, Current status and outlook on the clinical translation of biodegradable metals, Mater. Today 23 (March) (2019) 57–71, https://doi.org/10.1016/j.mattod.2018.05.018.

[20] M. Schinhammer, A.C. Hänzi, J.F. Löffler, P.J. Uggowitzer, Design strategy for biodegradable Fe-based alloys for medical applications, Acta Biomater. 6 (5) (2010) 1705–1713, https://doi.org/10.1016/j.actbio.2009.07.039.

[21] A. Francis, Y. Yang, S. Virtanen, A.R. Boccaccini, Iron and iron-based alloys for temporary cardiovascular applications, J. Mater. Sci. Mater. Med. 26 (3) (2015) 1–16, https://doi.org/10.1007/s10856-015-5473-8.

[22] H. Li, Y. Zheng, L. Qin, Progress of biodegradable metals, Prog. Nat. Sci. Mater. Int. 24 (5) (2014) 414–422, https://doi.org/10.1016/j.pnsc.2014.08.014.

[23] M. Peuster, P. Wohlsein, M. Brügmann, M. Ehlerding, K. Seidler, C. Fink, H. Brauer, A. Fischer, G. Hausdorfet, A novel approach to temporary stenting: degradable cardiovascular stents produced from corrodible metal - results 6-18 months after implantation into New Zealand white rabbits, Heart 86 (5) (2001) 563–569, https://doi.org/10.1136/heart.86.5.563.
[24] R. Waksman, R. Pakala, R. Baffour, R. Seabron, D. Hellinga, F.O. Tio, Short-term effects of biocorrodible iron stents in porcine coronary arteries, J. Intervent. Cardiol. 21 (1) (2008) 15–20, https://doi.org/10.1111/j.1540-8183.2007.00319.x.
[25] M. Peuster, C. Hesse, T. Schloo, C. Fink, P. Beerbaum, C. von Schnakenburg, Long-term biocompatibility of a corrodible peripheral iron stent in the porcine descending aorta, Biomaterials 27 (28) (2006) 4955–4962, https://doi.org/10.1016/j.biomaterials.2006.05.029.
[26] H. Hermawan, A. Purnama, D. Dube, J. Couet, D. Mantovani, Fe-Mn alloys for metallic biodegradable stents: degradation and cell viability studies, Acta Biomater. 6 (5) (2010) 1852–1860, https://doi.org/10.1016/j.actbio.2009.11.025.
[27] T. Kraus, F. Moszner, S. Fischerauer, M. Fiedler, E. Martinelli, J. Eichler, F. Witte, E. Willbold, M. Schinhammer, M. Meischel, P.J. Uggowitzer, J.F. Löffler, A. Weinberg, Biodegradable Fe-based alloys for use in osteosynthesis: outcome of an in vivo study after 52 weeks, Acta Biomater. 10 (7) (2014) 3346–3353, https://doi.org/10.1016/j.actbio.2014.04.007.
[28] S. Zhu, N. Huang, L. Xu, Y. Zhang, H. Liu, Y. Lei, H. Sun, Y. Yao, Biocompatibility of Fe-O films synthesized by plasma immersion ion implantation and deposition, Surf. Coating. Technol. 203 (10–11) (2009) 1523–1529, https://doi.org/10.1016/j.surfcoat.2008.11.033.
[29] H. Chen, E. Zhang, K. Yang, Microstructure, corrosion properties and bio-compatibility of calcium zinc phosphate coating on pure iron for biomedical application, Mater. Sci. Eng. C 34 (1) (2014) 201–206, https://doi.org/10.1016/j.msec.2013.09.010.
[30] M. Moravej, A. Purnama, M. Fiset, J. Couet, D. Mantovani, Electroformed pure iron as a new biomaterial for degradable stents: in vitro degradation and preliminary cell viability studies, Acta Biomater. 6 (5) (2010) 1843–1851, https://doi.org/10.1016/j.actbio.2010.01.008.
[31] D.T. Chou, D. Wells, D. Hong, B. Lee, H. Kuhn, P.N. Kumta, Novel processing of iron-manganese alloy-based biomaterials by inkjet 3-D printing, Acta Biomater. 9 (10) (2013) 8593–8603, https://doi.org/10.1016/j.actbio.2013.04.016.
[32] I. Costa, M.C.L. Oliveira, H.G. De Melo, R.N. Faria, The effect of the magnetic field on the corrosion behavior of Nd-Fe-B permanent magnets, J. Magn. Magn Mater. 278 (3) (2004) 348–358, https://doi.org/10.1016/j.jmmm.2003.12.1320.
[33] H. Hermawan, D. Dubé, D. Mantovani, Degradable metallic biomaterials: design and development of Fe-Mn alloys for stents, J. Biomed. Mater. Res., Part A 93 (1) (2010) 1–11, https://doi.org/10.1002/jbm.a.32224.
[34] P. Sharma, K.G. Jain, P.M. Pandey, S. Mohanty, In vitro degradation behaviour, cytocompatibility and hemocompatibility of topologically ordered porous iron scaffold prepared using 3D printing and pressureless microwave sintering, Mater. Sci. Eng. C 106 (2020), https://doi.org/10.1016/j.msec.2019.110247.
[35] A.M. Roman, V. Geantă, R. Cimpoeșu, C. Munteanu, N.M. Lohan, G. Zegan, E. R. Cernei, I. Ioniță, N. Cimpoeșu, N. Ioanid, In-Vitro analysis of FeMn-Si smart biodegradable alloy, Materials 15 (2) (2022), https://doi.org/10.3390/ma15020568.
[36] D. Bian, L. Qin, W. Lin, D. Shen, H. Qi, X. Shi, G. Zhang, H. Liu, H. Yang, J. Wang, D. Zhang, Y. Zheng, Magnetic resonance (MR) safety and compatibility of a novel iron bioresorbable scaffold, Bioact. Mater. 5 (2) (2020) 260–274, https://doi.org/10.1016/j.bioactmat.2020.02.011.
[37] N.S. Perov, P.M. Sheverdyaeva, M. Inoue, Investigations of the magnetic field effect on electrochemical processes, J. Magn. Magn Mater. 272–276 (III) (2004) 2448–2449, https://doi.org/10.1016/j.jmmm.2003.12.856.
[38] L.S.H. Nasher, Study the effect of magnetic field on the corrosion of steel in sodium chloride solution (NaCl), Misan Journal for Academic Studies 9 (17) (2010) 30–38.
[39] R. Sueptitz, J. Koza, M. Uhlemann, A. Gebert, L. Schultz, Magnetic field effect on the anodic behaviour of a ferromagnetic electrode in acidic solutions, Electrochim. Acta 54 (8) (2009) 2229–2233, https://doi.org/10.1016/j.electacta.2008.10.055.
[40] M. Sagawa, Effect of a local magnetic field on the dissolution of copper and iron in nitric acid solution, Trans. Japan Inst. Met. 23 (1) (1982) 38–40, https://doi.org/10.2320/matertrans1960.23.38.
[41] R. Wardan, S.R. Shamsudin, M.F.M. Wahid, M.S. Sanusi, Effect of pulse frequencies on low carbon steel in 3.5 wt% NaCl solution under zero charge corrosion protection, IOP Conf. Ser. Mater. Sci. Eng. 957 (1) (Oct. 2020) 012053, https://doi.org/10.1088/1757-899X/957/1/012053.
[42] P. Pouponneau, O. Savadogo, T. Napporn, L. Yahia, S. Martel, Corrosion study of single crystal Ni–Mn–Ga alloy and Tb0.27Dy0.73Fe1.95 alloy for the design of new medical microdevices, J. Mater. Sci. Mater. Med. 22 (2) (Feb. 2011) 237–245, https://doi.org/10.1007/s10856-010-4206-2.
[43] M. Multigner, C. Paternoster, A.J. López, M. Muñoz, M. Lieblich, B. Torres, D. Mantovani.Effect of magnetic field in the biocorrosion of ferrous biometals, Proceedings of the 11th International Symposium on Biodegradable Metals for Biomedical Applications, Biometal, Alicante, 2019.
[44] Z. Liu, Y. Yang, C. Shuai, C. He, Magnetic energy drives mass transfer processes to accelerate the degradation of Fe-based implant, Sustain. Mater. Technol. 38 (Dec. 2023) e00714, https://doi.org/10.1016/j.susmat.2023.e00714.
[45] S. Gambaro, C. Paternoster, B. Occhionero, J. Fiocchi, C.A. Biffi, A. Tuissi, D. Mantovani, Mechanical and degradation behavior of three Fe-Mn-C alloys for potential biomedical applications, Mater. Today Commun. 27 (February) (2021) 102250, https://doi.org/10.1016/j.mtcomm.2021.102250.
[46] ASTM, G31: standard practice for laboratory immersion corrosion testing of metals, Annual Book of ASTM Standards," An Am. Natl. Stand. 3.02 (February) (2021) 10 [Online]. Available: https://www.astm.org/standards/g31.
[47] E. Mouzou, C. Paternoster, R. Tolouei, A. Purnama, P. Chevallier, D. Dubé, F. Prima, D. Mantovani, In vitro degradation behavior of Fe-20Mn-1.2C alloy in three different pseudo-physiological solutions, Mater. Sci. Eng. C 61 (2016) 564–573, https://doi.org/10.1016/j.msec.2015.12.092.
[48] R. Tolouei, J. Harrison, C. Paternoster, S. Turgeon, P. Chevallier, D. Mantovani, The use of multiple pseudo-physiological solutions to simulate the degradation behavior of pure iron as a metallic resorbable implant: a surface-characterization study, Phys. Chem. Chem. Phys. 18 (29) (2016) 19637–19646, https://doi.org/10.1039/c6cp02451c.
[49] K.B. Baltzis, The FEMM package: a simple, fast, and accurate open source electromagnetic tool in science and engineering, J. Eng. Sci. Technol. Rev. 1 (1) (Jun. 2008) 83–89, https://doi.org/10.25103/jestr.011.18.
[50] A. Ghofur, D.A. Rachman, M.M. Lutfi, F. Rahman, The influence of leachate water on corrosion rate of mild steel plate, Int. J. Mech. Eng. Technol. Appl. 2 (2) (Jul. 2021) 137, https://doi.org/10.21776/MECHTA.2021.002.02.7.
[51] A.U. Syed, N.J. Simms, J.E. Oakey, Fireside corrosion of superheaters : effects of air and oxy-firing of coal and biomass, Fuel 101 (2012) 62–73, https://doi.org/10.1016/j.fuel.2011.03.010.
[52] N. Abu-warda, A.J. López, F. Pedraza, M. V Utrilla, Fireside corrosion on T24 steel pipes and HVOF NiCr coatings exposed to di ff erent salt mixtures, Corrosion Sci. 173 (May) (2020) 108747, https://doi.org/10.1016/j.corsci.2020.108747.
[53] U.P. Nayak, J. Webel, V. Pesnel, F. Mücklich, M.A. Guitar, Development of a protective coating for evaluating the sub-surface microstructure of a worn material, Tribol. Lett. 69 (4) (2021) 1–13, https://doi.org/10.1007/s11249-021-01541-8.
[54] S. Yagi, H. Oshima, K. Murase, E. Matsubara, Y. Awakura, Electrochemical iron-chromium alloying of carbon steel surface using alternating pulsed electrolysis, Mater. Trans. 49 (6) (2008) 1346–1354, https://doi.org/10.2320/matertrans.MRA2008028.
[55] M.C. Biesinger, B.P. Payne, A.P. Grosvenor, L.W.M. Lau, A.R. Gerson, R.S.C. Smart, Resolving surface chemical states in XPS analysis of first row transition metals, oxides and hydroxides: Cr, Mn, Fe, Co and Ni, Appl. Surf. Sci. 257 (7) (2011) 2717–2730, https://doi.org/10.1016/j.apsusc.2010.10.051.
[56] A.P. Grosvenor, B.A. Kobe, M.C. Biesinger, N.S. McIntyre, Investigation of multiplet splitting of Fe 2p XPS spectra and bonding in iron compounds, Surf. Interface Anal. 36 (12) (2004) 1564–1574, https://doi.org/10.1002/sia.1984.
[57] R. Zhang, D. Wang, L.C. Qin, G. Wen, H. Pan, Y. Zhang, N. Tian, Y. Zhou, X. Huang, MnCO3/Mn3O4/reduced graphene oxide ternary anode materials for lithium-ion batteries: facile green synthesis and enhanced electrochemical performance, J. Mater. Chem. A 5 (32) (2017) 17001–17011, https://doi.org/10.1039/c7ta02874a.
[58] P. Plate, C. Höhn, U. Bloeck, P. Bogdanoff, S. Fiechter, F.F. Abdi, R. van de Krol, A. C. Bronnebergal, On the origin of the OER activity of ultrathin manganese oxide films, ACS Appl. Mater. Interfaces 13 (2) (2021) 2428–2436, https://doi.org/10.1021/acsami.0c15977.
[59] Č. Donik, A. Kocijan, I. Paulin, M. Hočevar, P. Gregorčič, M. Godec, Improved biodegradability of Fe–Mn alloy after modification of surface chemistry and topography by a laser ablation, Appl. Surf. Sci. 453 (March) (2018) 383–393, https://doi.org/10.1016/j.apsusc.2018.05.066.
[60] V. Wagener, S. Virtanen, Protective layer formation on magnesium in cell culture medium, Mater. Sci. Eng. C 63 (Jun. 2016) 341–351, https://doi.org/10.1016/j.msec.2016.03.003.
[61] J. Zhou, M. Fink, M. Bruns, Y. Yang, R. Detsch, A.R. Boccaccini, H. Ermert, S. Virtanen, Modification of in vitro degradation behavior of pure iron with ultrasonication treatment: comparison of two different pseudo-physiological solutions, Mater. Sci. Eng. C 95 (Feb. 2019) 275–285, https://doi.org/10.1016/j.msec.2018.10.079.
[62] J. Zhou, Y. Yang, M. Alonso Frank, R. Detsch, A.R. Boccaccini, S. Virtanen, Accelerated degradation behavior and cytocompatibility of pure iron treated with sandblasting, ACS Appl. Mater. Interfaces 8 (40) (Oct. 2016) 26482–26492, https://doi.org/10.1021/acsami.6b07068.
[63] H. Hu, J.Y. Xu, H. Yang, J. Liang, S. Yang, H. Wu, Morphology-controlled hydrothermal synthesis of MnCO3 hierarchical superstructures with Schiff base as stabilizer, Mater. Res. Bull. 46 (11) (2011) 1908–1915, https://doi.org/10.1016/j.materresbull.2011.07.028.
[64] A. Chiba, T. Ogawa, Influence of magnetic field on the dissolution of copper, zinc and brass in flowing nitric acid solution, Corros. Eng. 38 (10) (1989) 523–528, https://doi.org/10.3323/jcorr1974.38.10_523.
[65] A. Chiba, K. Kawazu, O. Nakano, T. Tamura, S. Yoshihara, E. Sato, The effects of magnetic fields on the corrosion of aluminum foil in sodium chloride solutions, Corrosion Sci. 36 (3) (Mar. 1994) 539–543, https://doi.org/10.1016/0010-938X(94)90042-6.
[66] S. Zhao, Z. You, X. Zhang, J. Li, Magnetic field effects on the corrosion and electrochemical corrosion of Fe83Ga17 alloy, Mater. Char. 174 (October 2020) (2021) 110994, https://doi.org/10.1016/j.matchar.2021.110994.
[67] Z.-P. Lu, J.-M. Chen, Magnetic field effects on anodic polarisation behaviour of iron in neutral aqueous solutions, Br. Corrosion J. 35 (3) (Mar. 2000) 224–228, https://doi.org/10.1179/000705900101501281.
[68] G. Hinds, J.M.D. Coey, M.E.G. Lyons, Influence of magnetic forces on electrochemical mass transport, Electrochem. Commun. 3 (5) (2001) 215–218, https://doi.org/10.1016/S1388-2481(01)00136-9.
[69] H. Uppili, B. Daglen, Bi-directional giant magneto impedance sensor, Adv. Mater. Phys. Chem. 3 (5) (2013) 249–254, https://doi.org/10.4236/ampc.2013.35036.

[70] Y.C. Tang, A.J. Davenport, Magnetic field effects on the corrosion of artificial pit electrodes and pits in thin films, J. Electrochem. Soc. 154 (7) (2007) C362, https://doi.org/10.1149/1.2736662.
[71] R. Sueptitz, K. Tschulik, M. Uhlemann, L. Schultz, A. Gebert, Effect of high gradient magnetic fields on the anodic behaviour and localized corrosion of iron in sulphuric acid solutions, Corrosion Sci. 53 (10) (2011) 3222–3230, https://doi.org/10.1016/j.corsci.2011.05.070.
[72] K.M. Grant, J.W. Hemmert, H.S. White, Magnetic focusing of redox molecules at ferromagnetic microelectrodes, Electrochem. Commun. 1 (8) (Aug. 1999) 319–323, https://doi.org/10.1016/S1388-2481(99)00065-X.
[73] Y. Tanimoto, H. Yano, S. Watanabe, A. Katsuki, W. Duan, M. Fujiwara, Effect of high magnetic field on copper deposition from an aqueous solution, Bull. Chem. Soc. Jpn. 73 (4) (Apr. 2000) 867–872, https://doi.org/10.1246/bcsj.73.867.
[74] S.J. Ling, J. Sanny, W. Moebs, D. Janzen, Introduction to Electricity, Magnetism, and Circuits – Open Textbook, 2018, pp. 794–795 [Online]. Available: https://openpress.usask.ca/physics155/.
[75] O. Lioubashevski, E. Katz, I. Willner, Magnetic field effects on electrochemical processes: a theoretical hydrodynamic model, J. Phys. Chem. B 108 (18) (2004) 5778–5784, https://doi.org/10.1021/jp037785q.
[76] R. Oriňaková, R. Gorejová, M. Petráková, Z.O. Králová, A. Oriňak, M. Kupková, M. Hrubovčáková, M. Podobová, M. Baláž, R.M. Smith, Degradation performance of open-cell biomaterials from phosphated carbonyl iron powder with PEG coating, Materials 13 (18) (2020) 10–13, https://doi.org/10.3390/ma13184134.
[77] T. Huang, Y. Zheng, Y. Han, Accelerating degradation rate of pure iron by zinc ion implantation, Regen. Biomater. 3 (4) (2016) 205–215, https://doi.org/10.1093/RB/RBW020.
[78] Y. Qi, H. Qi, Y. He, W. Lin, P. Li, L. Qin, Y. Hu, L. Chen, Q. Liu, H. Sun, Q. Liu, G. Zhang, S. Cui, J. Hu, L. Yu, D. Zhang, J. Ding, Strategy of metal–polymer composite stent to accelerate biodegradation of iron-based biomaterials, ACS Appl. Mater. Interfaces 10 (1) (Jan. 2018) 182–192, https://doi.org/10.1021/acsami.7b15206.
[79] E. Mouzou, et al., In vitro degradation behavior of Fe–20Mn–1.2C alloy in three different pseudo-physiological solutions, Mater. Sci. Eng. C 61 (Apr. 2016) 564–573, https://doi.org/10.1016/j.msec.2015.12.092.
[80] T.M. Peev, Electrochemical processes in magnetic field, Bulg. Chem. Commun. 40 (3) (2008) 190–197.
[81] M. Salama, M.F. Vaz, R. Colaço, C. Santos, M. Carmezim, Biodegradable iron and porous iron: mechanical properties, degradation behaviour, manufacturing routes and biomedical applications, J. Funct. Biomater. 13 (2) (2022), https://doi.org/10.3390/jfb13020072.
[82] R. Gorejová, L. Haverová, R. Oriňaková, A. Oriňak, M. Oriňak, Recent advancements in Fe-based biodegradable materials for bone repair, J. Mater. Sci. 54 (3) (2019) 1913–1947, https://doi.org/10.1007/s10853-018-3011-z.
[83] H. Dong, F. Lin, A.R. Boccaccini, S. Virtanen, Corrosion behavior of biodegradable metals in two different simulated physiological solutions: comparison of Mg, Zn and Fe, Corrosion Sci. 182 (December 2020) (2021) 109278, https://doi.org/10.1016/j.corsci.2021.109278.
[84] E. Zhang, H. Chen, F. Shen, Biocorrosion properties and blood and cell compatibility of pure iron as a biodegradable biomaterial, J. Mater. Sci. Mater. Med. 21 (7) (2010) 2151–2163, https://doi.org/10.1007/s10856-010-4070-0.
[85] R. Tolouei, J. Harrison, C. Paternoster, S. Turgeon, P. Chevallier, D. Mantovani, The use of multiple pseudo-physiological solutions to simulate the degradation behavior of pure iron as a metallic resorbable implant: a surface-characterization study, Phys. Chem. Chem. Phys. 18 (29) (2016) 19637–19646, https://doi.org/10.1039/C6CP02451C.
[86] Y. Gu, M. Yoshikiyo, A. Namai, D. Bonvin, A. Martinez, R. Piñol, P. Téllez, N.J. O. Silva, F. Ahrentorp, C. Johansson, J. Marco-Brualla, R. Moreno-Loshuertos, P. Fernández-Silva, Y. Cui, S. Ohkoshi, A. Millán, Magnetic hyperthermia with ε-Fe 2 O 3 nanoparticles, RSC Adv. 10 (48) (2020) 28786–28797, https://doi.org/10.1039/D0RA04361C.
[87] J. Huang, A. Gonzalez Orive, J.T. Krüger, K.-P. Hoyer, A. Keller, G. Grundmeier, Influence of proteins on the corrosion of a conventional and selective laser beam melted FeMn alloy in physiological electrolytes, Corrosion Sci. 200 (May 2022) 110186, https://doi.org/10.1016/j.corsci.2022.110186.
[88] Y. Chen, T. Fitchorov, J. Gao, A. Koblischka-Veneva, M.R. Koblischka, C. Vittoria, V.G. Harris, Topochemical growth of textured polycrystalline barium hexaferrite from oriented antiferromagnetic α-FeOOH nanorods, Nanotechnology 20 (44) (2009) 445606, https://doi.org/10.1088/0957-4484/20/44/445606.
[89] A.S. Ulrich, U. Glatzel, M.C. Galetz, Discontinuities in oxidation kinetics: a new model and its application to Cr–Si-base alloys, Oxid. Metals 95 (5–6) (2021) 445–465, https://doi.org/10.1007/s11085-021-10029-8.
[90] A.H. Heuer, H. Kahn, F. Ernst, G.M. Michal, D.B. Hovis, R.J. Rayne, F.J. Martin, P. M. Natishan, Enhanced corrosion resistance of interstitially hardened stainless steel: implications of a critical passive layer thickness for breakdown, Acta Mater. 60 (2) (Jan. 2012) 716–725, https://doi.org/10.1016/j.actamat.2011.10.004.
[91] A. Schreiber, J.W. Schultze, M.M. Lohrengel, F. Kármán, E. Kálmán, Grain dependent electrochemical investigations on pure iron in acetate buffer pH 6.0, Electrochim. Acta 51 (13) (2006) 2625–2630, https://doi.org/10.1016/j.electacta.2005.07.052.
[92] J.H. Seo, J.-H. Ryu, D.N. Lee, Formation of crystallographic etch pits during AC etching of aluminum, J. Electrochem. Soc. 150 (9) (2003) B433, https://doi.org/10.1149/1.1596952.
[93] X.X. Wei, B. Zhang, B. Wu, Y.J. Wang, X.H. Tian, L.X. Yang, E.E. Oguzie, X.L. Ma, Enhanced corrosion resistance by engineering crystallography on metals, Nat. Commun. 13 (1) (2022), https://doi.org/10.1038/s41467-022-28368-8.
[94] S. Shaikh, N.A. Lapin, B. Prasad, C.R. Sturge, C. Pybus, R. Pifer, Q. Wang, B. M. Evers, R. Chopra, D.E. Greenberg, Intermittent alternating magnetic fields diminish metal-associated biofilm in vivo, Sci. Rep. 13 (1) (Dec. 2023) 22456, https://doi.org/10.1038/s41598-023-49660-7.
[95] Q. Wang, J. Vachon, B. Prasad, C.A. Pybus, N. Lapin, R. Chopra, D.E. Greenberg, Alternating magnetic fields and antibiotics eradicate biofilm on metal in a synergistic fashion, npj Biofilms Microbiomes 7 (1) (Aug. 2021) 68, https://doi.org/10.1038/s41522-021-00239-y.
[96] ASTAR, Available from URL: https://astar.eu/products/physiomg-827, 2024.